ADVANCING EARTH AND SPACE SCIENCES

JGR Earth Surface

RESEARCH ARTICLE

10.1029/2024JF008118

Key Points:

- A workflow is developed to extract fracture vertical measurements from ICESat-2 photon data applied to the Thwaites Ice Shelf (2018–2024)
- The fracture depth/freeboard ratio derived from ICESat-2 data provides a quantitative metric for characterizing vertical structural damage
- Increased fracturing and flow on the eastern section of Thwaites degrade ice-shelf structural integrity, contrasting with the western part

Supporting Information:

Supporting Information may be found in the online version of this article.

Correspondence to:

S. Wang,
skw5660@psu.edu

Citation:

Wang, S., Alexander, P. M., Alley, R. B., Huang, Z., Parizek, B. R., Willet, A. G., & Anandakrishnan, S. (2025). Recent variability in fracture characteristics and ice flow of Thwaites Ice Shelf, West Antarctica. *Journal of Geophysical Research: Earth Surface*, *130*, e2024JF008118. https://doi.org/10.1029/2024JF008118

Received 25 OCT 2024
Accepted 5 MAY 2025

Author Contributions:

Conceptualization: Shujie Wang, Patrick M. Alexander, Richard B. Alley, Byron R. Parizek
Data curation: Shujie Wang, Patrick M. Alexander, Zhengrui Huang
Formal analysis: Shujie Wang, Patrick M. Alexander, Richard B. Alley, Zhengrui Huang, Byron R. Parizek
Funding acquisition: Shujie Wang
Investigation: Shujie Wang, Patrick M. Alexander, Richard B. Alley, Zhengrui Huang, Byron R. Parizek
Methodology: Shujie Wang, Patrick M. Alexander
Project administration: Shujie Wang

Recent Variability in Fracture Characteristics and Ice Flow of Thwaites Ice Shelf, West Antarctica

Shujie Wang[1,2], Patrick M. Alexander[3], Richard B. Alley[2,4], Zhengrui Huang[1], Byron R. Parizek[4,5], Amanda G. Willet[4], and Sridhar Anandakrishnan[2,4]

[1]Department of Geography, The Pennsylvania State University, University Park, PA, USA, [2]Earth and Environmental Systems Institute, The Pennsylvania State University, University Park, PA, USA, [3]Lamont-Doherty Earth Observatory, Columbia University, Palisades, NY, USA, [4]Department of Geosciences, The Pennsylvania State University, University Park, PA, USA, [5]Mathematics and Geosciences, The Pennsylvania State University, DuBois, PA, USA

Abstract The rapidly changing Thwaites Ice Shelf is crucial for understanding ice-shelf dynamical processes and their implications for sea-level rise from Antarctica. Fractures, particularly their vertical structure, are key to ice-shelf structural integrity but remain poorly measured. To address this, we developed a fracture-characterization workflow using ICESat-2 ATL03 geolocated photon heights, producing the first time-series vertical measurements of fractures across Thwaites from 2018 to 2024. We introduced the fracture depth/freeboard ratio as a normalized metric to quantify vertical fracture extent, serving as an indicator of structural damage. This metric enabled us to track fracture evolution in both the eastern ice shelf and western glacier tongue. In the eastern section, fracturing intensified along the northwestern shear zone and near the grounding line, in a positive feedback loop between enhanced fracturing and accelerated flow. The western section maintained an active rift formation zone about 15 km downstream of the historical grounding line. Flow velocity changes in this section were primarily confined to the unconstrained downstream portion, exhibiting an overall deceleration trend, while the upstream area remained stable. This contrast highlights the role of lateral margin conditions in governing ice-shelf fracture and flow behavior. Changes in the eastern section showed some correspondence with warm winter air temperatures, reduced sea ice, and persistent warm ocean anomalies at shallower depths, suggesting that atmosphere-sea ice-ocean interactions influence ice-shelf structural integrity through basal processes. Future research should integrate satellite-derived fracture observations with numerical models of ice fracture and flow to better capture the dynamics of ice-shelf weakening and retreat.

Plain Language Summary Understanding the processes driving changes in Antarctic ice shelves is crucial for assessing how Antarctica will evolve and impact global sea levels. Modeling ice-shelf retreat is complex, especially due to limited data on ice fracturing. This challenge is pronounced at the Thwaites Ice Shelf in West Antarctica, which is known for its rapid changes, fractured surface, and fast ice flow. NASA's ICESat-2 satellite allows us to examine ice-shelf fractures with unprecedented detail. We developed an advanced workflow to extract vertical fracture measurements from ICESat-2 data, providing the first record of how fractures evolved vertically over time in this region from 2018 to 2024. The eastern section experienced increased fracturing coupled with accelerated flow, creating a self-reinforcing feedback loop that further weakened the ice shelf. The western section behaved differently, remaining relatively stable overall, with flow changes primarily restricted to its downstream portions. Warmer winter air temperatures, reduced sea ice, and warmer ocean water at shallow depths may have contributed to fracture growth and accelerated ice flow in vulnerable parts of the ice shelf. Our study provides a new approach to measure ice-shelf fractures and highlights the importance of fracture-flow interactions for predicting the future behavior of Antarctic ice shelves.

1. Introduction

Fractures play a crucial role in the structural integrity of glaciers and ice shelves, influencing their mechanical properties, flow dynamics, and calving behavior (R. B. Alley et al., 2023; Benn et al., 2007; Benn & Åström, 2018; Bassis et al., 2024; Lhermitte et al., 2020). Observations of fracture types, spatial distribution, temporal changes, and morphological characteristics are essential for understanding and modeling their formation and propagation in response to varying internal stresses and external conditions. This knowledge is particularly important for investigating the mechanisms behind ice-shelf retreat and destabilization. Specifically, surface and

Resources: Shujie Wang, Richard B. Alley, Byron R. Parizek
Software: Shujie Wang
Supervision: Shujie Wang
Validation: Shujie Wang
Visualization: Shujie Wang, Patrick M. Alexander
Writing – original draft: Shujie Wang
Writing – review & editing: Shujie Wang, Patrick M. Alexander, Richard B. Alley, Zhengrui Huang, Byron R. Parizek, Amanda G. Willet, Sridhar Anandakrishnan

basal fractures on ice shelves can affect the ponding and drainage of surface meltwater, a factor vital for hydrofracturing processes (R. B. Alley et al., 2005; Banwell et al., 2013; Bell et al., 2018; Hughes, 1983; Lai et al., 2020; McGrath et al., 2012; Robel & Banwell, 2019; Weertman, 1973). Their vertical structures can further influence the formation and growth of rifts (Wang et al., 2021), which are through-cutting fractures that primarily govern the calving of large icebergs from Antarctic ice shelves (Fricker et al., 2005; Hulbe et al., 2010; Joughin, 2005; Lescarmontier et al., 2015; Olinger et al., 2024; Walker & Gardner, 2019; Wang et al., 2022). The sudden and dramatic disintegration of the northern Larsen Ice Shelf in the eastern Antarctic Peninsula was preceded by noticeable changes in the amount, type, and distribution of fractures (Doake et al., 1998; Glasser & Scambos, 2008; MacAyeal et al., 2003; Scambos et al., 2004; Wang et al., 2023). Therefore, fracture properties and their evolution over time are key factors to consider when modeling ice-shelf dynamics. Improved representations of fractures could be included in ice-shelf models to increase their ability to accurately project sea-level change (e.g., DeConto & Pollard, 2016; DeConto et al., 2021; Edwards et al., 2021; Kopp et al., 2017; Nowicki et al., 2020; Ritz et al., 2015; Seroussi et al., 2020).

Fracture depth is a critical parameter for describing ice damage and modeling calving (e.g., Benn et al., 2007; Nick et al., 2010; Pollard et al., 2015; Sun et al., 2017). Typically, fracture depth is inferred using assumptions about ice mechanics and material properties (e.g., Nye, 1957; van der Veen, 1998; Weertman, 1973) rather than being calibrated against actual observations due to the general lack of measurements capable of constraining vertical fracture structure. This knowledge gap is partly due to the limitations of earlier satellite remote sensing technologies, which did not provide the precision required to resolve fracture features in fine detail. Traditional satellite radar altimeters, with footprint sizes ranging from several to tens of kilometers (Brenner et al., 2007), lacked this precision. Very high-resolution satellites, such as the WorldView series, offer stereo capabilities for producing digital elevation models with meter-level resolution (e.g., REMA, Howat et al., 2019). However, optical imagery-based photogrammetry techniques used for surface height retrieval can be affected by shadows cast by fracture walls. The recent launch of NASA's Ice, Cloud, and Land Elevation Satellite-2 (ICESat-2) has enabled the extraction of vertical information on ice fractures directly from space (e.g., Herzfeld et al., 2021; Li et al., 2021; Walker & Gardner, 2019; Wang et al., 2021). ICESat-2, launched in September 2018, is equipped with the Advanced Topographic Laser Altimeter System, which emits green laser pulses for surface height measurements (Markus et al., 2017). The high resolution and dense sampling of ICESat-2 (~13 m footprint size, 0.7 m along-track sampling distance) enable the characterization of very fine structures, such as canopies, ice fractures, and iceberg shapes (e.g., Narine et al., 2022; Walker et al., 2021; Walker & Gardner, 2019; Wang et al., 2021). Although ICESat-2 ATL03 photon height measurements (Neumann et al., 2019) provide unprecedented detail, utilizing raw photon data directly is challenging due to its vast data volume and inherent noise. Therefore, these geolocated photon height measurements are processed into advanced data products for specific scientific objectives, such as ATL06 for land ice (Smith et al., 2019) and ATL10 for sea ice (Kwok et al., 2020). The ATL06 data product was recently used to derive the vertical structure of large transverse fractures over the Amery Ice Shelf (Wang et al., 2021), demonstrating the great potential of ICESat-2 for fracture research. However, ATL06 data, which aggregate along-track photon heights into overlapping segments (Smith et al., 2019), has limitations in detecting small-scale fractures and may underestimate vertical depth due to its intrinsic smoothing effect. This issue is particularly problematic when investigating topographically complex, heavily fractured, and rapidly changing areas such as the Thwaites Ice Shelf.

The Thwaites Ice Shelf (Figure 1a) in West Antarctica constrains the ice flow from the Thwaites Glacier. This glacier, about 120 km wide, could contribute up to 65 cm to sea-level rise from its modern drainage area, and more from interconnections through interior basins of the ice sheet (Joughin & Alley, 2011; Scambos et al., 2017). Influenced by the warm Circumpolar Deep Water (CDW) in the Amundsen Sea (Jenkins et al., 2018; Nakayama et al., 2019; Parizek et al., 2013; Seroussi et al., 2017; Thoma et al., 2008), this glacier-ice shelf system has experienced rapid changes in recent decades, including front retreat, flow acceleration, ice thinning, and grounding line retreat (Andreasen et al., 2023; Joughin et al., 2014; Miles et al., 2020; Milillo et al., 2019; Paolo et al., 2018; Rabus et al., 2003; Rignot et al., 2014; Schmidt et al., 2023; Smith et al., 2020). Satellite imagery reveals the dense distribution, spatial heterogeneity, and rapid evolution of fracture patterns in this area (K. E. Alley et al., 2021a; R. B. Alley et al., 2021b; Benn et al., 2022; Lhermitte et al., 2020; Surawy-Stepney et al., 2023). While previous studies have primarily focused on the spatial distribution and extent of fractures from a qualitative perspective, their vertical structure and temporal evolution remain poorly understood, and vertical fracture measurements have not yet been extensively retrieved for this region.

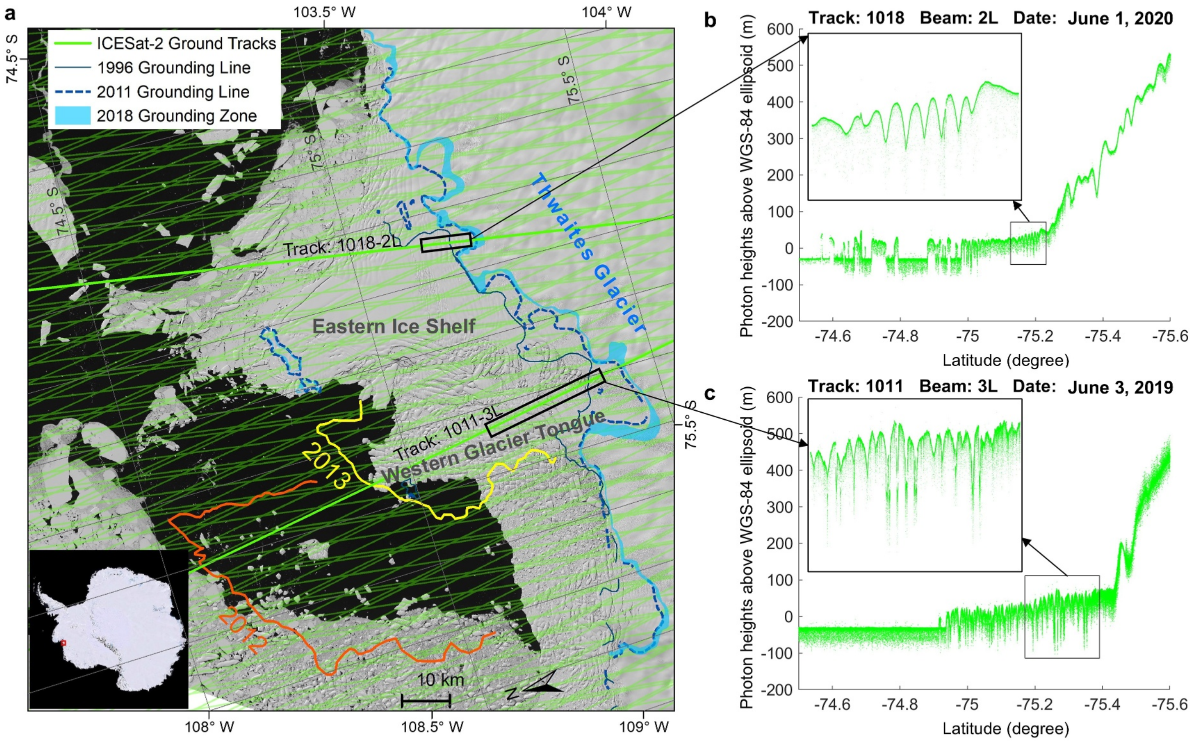

Figure 1. (a) Thwaites Ice Shelf. Imagery is from the panchromatic band of a Landsat-8 image acquired on 13 February 2019. The 1996 and 2011 grounding lines are from the MEaSUREs Antarctic Grounding Line from Differential Satellite Radar Interferometry (Version 2) data set (Rignot et al., 2016). The 2018 grounding zones are from the MEaSUREs Grounding Zone of the Antarctic Ice Sheet (Version 1) data set (Rignot et al., 2023). The orange and yellow lines represent the ice-front positions for the western glacier tongue in 2012 and 2013, respectively. Green lines indicate ICESat-2 data tracks, with tracks 1,018 (beam 2 L, strong beam) and 1,011 (beam 3 L, strong beam) highlighted. (b) ATL03 photon height data (confidence flag >0) from Track 1,018 (beam 2 L, strong beam) over the eastern ice shelf, acquired on 1 June 2020. (c) ATL03 photon height data (confidence flag >0) from Track 1,011 (beam 3 L, strong beam) over the western glacier tongue, acquired on 3 June 2019.

In this study, we addressed the gap in fracture measurement by developing a workflow to extract vertical fracture measurements from ICESat-2 ATL03 photon height data, a method that can be generalized for use in other regions. Specifically, this workflow includes a Multiscale Adaptive Binary Segmentation (MABS) approach, which generates surface elevation profiles from ICESat-2 geolocated photon data (ATL03) and adapts to the topographic complexity caused by various fracture structures. Additionally, an improved Hierarchical Object-Oriented Fracture Detection Algorithm (Wang et al., 2021) was applied to extract individual fractures from these elevation profiles. Applying this workflow to ICESat-2 ATL03 data collected between 2018 and 2024, we generated the first time-series of vertical fracture measurements over the complex Thwaites Ice Shelf. We analyzed the spatiotemporal characteristics of fracture patterns in both the eastern ice shelf and the western glacier tongue. Additionally, we examined fracture-flow variability by deriving ice flow velocity data for 24 seasons during the study period using Sentinel-1 imagery. Based on these velocity measurements, we analyzed the spatiotemporal variability of strain rates and linked them to the fracture measurements. To further understand these dynamics, we used climate reanalysis data sets to discuss the potential role of atmospheric and oceanic drivers, developing hypotheses and providing a comprehensive view of the factors influencing the vulnerability and future behavior of this critical region.

2. Study Area and Data

2.1. Study Area

The Thwaites Ice Shelf (Figure 1a) has two distinct sections: the eastern ice shelf, anchored by a seafloor ridge, and the unconstrained, heavily fractured western glacier tongue. Recent observations indicate a thinning trend in the eastern ice shelf and a gradual reduction in the extent of its pinning point (K. E. Alley et al., 2021a; R. B. Alley et al., 2021b; Wild et al., 2022, 2024). The western tongue retreated approximately 80 km from 2000 to 2018, transitioning from a structurally intact ice tongue to a fragmented assembly of ice blocks (Miles et al., 2020). This glacier tongue is characterized by a heavily crevassed surface, which differs from the typical surface structure of Antarctic ice shelves and poses a challenge in resolving fracture structures from coarse-resolution surface elevation data. Figures 1b and 1c shows examples of ICESat-2 ATL03 data over the study area, highlighting the differences in surface structural complexity between these two sections.

2.2. Data

2.2.1. ICESat-2 Data

We used ICESat-2 Level 2 Global Geolocated Photon Data (ATL03) (Neumann et al., 2021, 2023), acquired between November 2018 and April 2024, to extract vertical fracture measurements. ICESat-2 provides photon height measurements from six beams arranged in three adjacent pairs, laterally offset by ∼3.3 km. Each pair consists of a strong beam and a weak beam, separated by ∼90 m, with different transmit energies to accommodate the varying reflectivity of surface types (e.g., bright snow vs. dark water). In this study, we utilized both strong and weak beams. The ATL03 data set provides time, latitude, longitude, height above the WGS-84 ellipsoid, and a confidence classification for each photon event (0 for noise, 1 for likely signal photon events, 2 for low-confidence signals, 3 for medium-confidence signals, and 4 for high-confidence signals). We excluded photon heights labeled with a confidence level of 0. For the ice-shelf areas, we applied dynamic atmospheric correction and ocean tide correction using the geophysical data provided in the ICESat-2 data set. To benchmark the performance of our approach, we compared a portion of our results with the Level 3 Land Ice Height (ATL06) product (Smith et al., 2019, 2021).

2.2.2. Sentinel-1 Satellite Imagery

For fracture location validation and ice flow velocity derivation, we used Sentinel-1A/B synthetic aperture radar (SAR) images accessed from the Alaska Satellite Facility data archive. Using Level-1 Ground Range Detected products, we generated backscatter coefficient images in the Sentinel Application Platform (SNAP) (Veci et al., 2014) through these processing steps: apply-orbit-file, radiometric calibration, terrain correction, and speckle noise reduction. We derived seasonal ice flow velocities for the 2018–2024 period using a feature tracking method based on image-matching (Liu et al., 2012; Scambos et al., 1992; Wang et al., 2016, 2022, 2023), which identifies and measures spatial displacements of trackable surface features. Based on the derived flow velocities, strain rates were subsequently calculated, as detailed in Section 4.3.

2.2.3. Atmosphere and Ocean Reanalysis Data

To explore potential linkages between fracture-flow variability and atmospheric and oceanic conditions, we used data sets from the ECMWF Reanalysis 5th Generation (ERA5) (Hersbach et al., 2020, 2023), provided on a 0.25° longitude-latitude grid, and the ECMWF Ocean Reanalysis System 5 (ORAS5) (Zuo et al., 2019), available on a ∼0.25° tripole grid, with a resolution of 0.25° longitude and 0.05°–0.08° latitude in the Thwaites region. Specifically, we utilized monthly depth-varying ocean potential temperature and salinity from ORAS5 and monthly averaged atmospheric variables from ERA5, including 2-m air temperature, 10-m wind speed components (u and v), and sea ice concentration. Monthly anomalies were calculated relative to the 1979–2010 baseline and aggregated into seasonal averages. Ocean data were vertically averaged over 10–200 m, 200–400 m, and 400–700 m depth ranges, with weighting based on layer thickness, which varies from ∼1 m near the surface to ∼200 m at depth. For regional variability, we focused on the area between 80° to 70°S and 120° to 100°W, centered on Thwaites. To analyze time series of atmospheric and sea ice variability, we computed averages over a smaller region (76.5° to 73.5°S, 110° to 104°W) also centered on Thwaites. For ocean variability, we examined two subregions with notable ocean anomalies: a region near the eastern ice shelf (75° to 74°S, 106° to 102°W), and a region near the western glacier tongue (75° to 74°S, 110° to 107.5°W). We note that reanalysis data may exhibit biases, particularly in regions with sparse observations. However, ERA5, the data set used in this study, is widely utilized and has demonstrated improved agreement with observations compared to its predecessor, ERA-Interim (Hersbach et al., 2020; Soci et al., 2024). Similarly, ORAS5 has shown better consistency with observations than ORAS4, particularly in sea surface temperature, sea level, and sea ice cover (Zuo et al., 2019).

3. Workflow for Fracture Characterization From ICESat-2 Photon Data

To address the existing gaps in fracture vertical measurements, we developed a two-step workflow to extract fracture structures from ICESat-2 satellite altimetry data, including (a) generating high-resolution surface elevation profiles from ICESat-2 photon heights, and (b) extracting fracture cross-sections from these high-resolution elevation profiles. Each step is described in detail below along with an evaluation of its performance.

3.1. Multiscale Adaptive Binary Segmentation (MABS) Approach

We developed a novel method, the MABS algorithm, to process ICESat-2 ATL03 photon heights and produce surface elevation profiles with variable resolution. This method adapts to local topographical features, effectively overcoming the limitations of ATL06 data, which tends to obscure finer-scale features in complex, heavily fractured areas. MABS dynamically adjusts its along-track sampling interval during the aggregation of photon measurements, adapting to topographical complexity. The resulting profile is similar to the ATL06 data but with a flexible sampling distance instead of a fixed interval. Specifically, the MABS algorithm enhances resolution (i.e., smaller sampling distance) to capture complex surfaces, such as fractured areas, while adopting a lower resolution for smoother terrains. This adaptive approach preserves the detailed structure of fractured areas and reduces data redundancy in less varied terrains. Similar adaptive strategies are employed in the density-dimension algorithm (DDA-Ice) (Herzfeld et al., 2021) and SlideRule (Shean et al., 2023), albeit with different implementation methods. In our approach, we use a binary segmentation method incorporating median-based metrics of central tendency and deviation.

Conceptually, ATL03 photon data can be visualized as a two-dimensional "photon cloud." To a human observer, the areas with maximum photon density can pinpoint the approximate location of the surface. The MABS algorithm leverages this intuitive characteristic by segmenting photons into a two-dimensional grid. Rather than using a fixed grid size for photon density calculations, we adopt a multiscale strategy analogous to building an image pyramid. This involves using a series of grids at different resolutions, starting with a coarse resolution grid. The algorithm is illustrated in Figure 2a and described in the following steps:

Step 1. Segment the photon cloud into a grid by initializing the grid cell size as X_0 along the data track direction (x direction) and Y_0 along the vertical height direction (y direction). Count the number of photons within each grid cell. For each sampling interval along the x-direction, select the grid cell with the highest number of photons within the vertical column. If this cell contains less than P_{sum} (e.g., 70%) of the total photons in the column, select additional grid cells with the next-highest photon counts until the cumulative number of selected photons exceeds P_{sum}. The goal is to identify the most probable surface locations at a coarse resolution by focusing on areas with the highest photon returns. Multiple grid cells may be selected within each x-interval if the topography has a significant height range, as expected for fractures.

Step 2. For each selected grid cell, compute the median of photon heights to estimate the surface height and calculate the median absolute deviation (MAD) to quantify the dispersion of photon heights within the grid cell. The median and MAD are used because they are less sensitive to outliers. A higher MAD value implies a more dispersed distribution of photon heights within a grid cell, indicating that the current grid size is too coarse to accurately capture the finer details of the surface topography.

Step 3. Perform iterative binary segmentation to generate a detailed surface elevation profile that adapts to varying topographical complexities. Subdivide the grid cells identified in Steps 1 and 2 into up to four smaller grid cells in the x and y directions based on specific criteria (detailed in Text S1 in Supporting Information S1), including the minimum number of photons per grid cell, minimum grid resolution (e.g., 2 m along the x-direction), MAD change, and median height variation. Segmentation stops for a grid cell if any of the criteria are met; otherwise, Steps 2 and 3 are repeated recursively until no grid cells qualify for segmentation. The resulting elevation profile is determined by the medians of photon heights within the final grid cells.

This adaptive strategy results in two scenarios: (a) in areas with complex topography, the algorithm refines the grid to a finer resolution, and (b) in areas with smoother terrain, the segmentation process stops earlier, generating a sparser set of points. Figure 2b compares the performance of the MABS algorithm to the ATL06 data, using Track 1,011 Beam 3 L (acquired on 3 June 2019, strong beam) as an example. Track 1,011 crosses the western glacier tongue, which is characterized by significant surface undulations caused by a complex mixture of

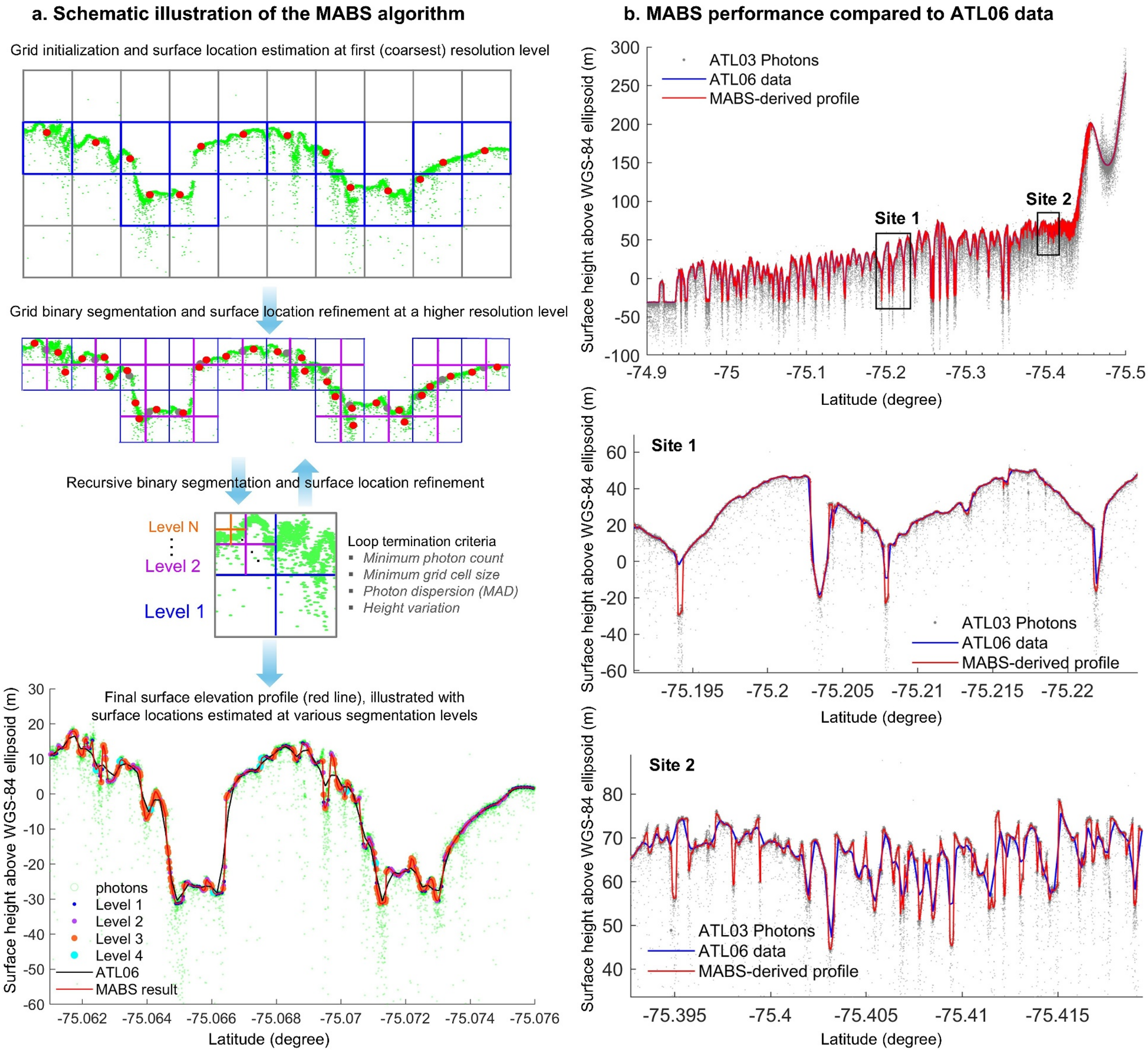

Figure 2. (a) Multiscale adaptive binary segmentation (MABS) algorithm workflow. (b) Illustration of MABS performance compared to ATL06 data using Track 1,011 beam 3 L data (3 June 2019) as an example, with a minimum resolution of 2 m along the *x*-direction.

fractures, icebergs, and ice mélange. The results show that MABS is particularly adept at defining fracture edges and tips, whereas ATL06 tends to overestimate surface heights in fractured areas due to its smoothing effect. Using MABS, we processed twenty ATL03 data tracks collected between November 2018 and April 2024 across the study area.

3.2. Improved Hierarchical Object-Oriented Fracture Detection Algorithm

We implemented an improved hierarchical object-oriented fracture detection algorithm to extract cross-sections of fracture features from the MABS-derived surface elevation profiles. Prior to fracture extraction, the MABS-derived surface heights were converted to geoid-referenced height values (EGM 2008). Originally developed by Wang et al. (2021), this algorithm builds upon the localized contour tree method (Wang et al., 2017; Wu et al., 2015), which is typically applied to extract hills or depressions from two-dimensional topographic data sets. For ICESat-2 along-track data, our goal is to identify depression features with fracture morphologies within one-dimensional elevation profiles. The core principle of the algorithm involves an iterative process to detect all depression features, emulating a bottom-up water inundation process starting from the lowest elevation point.

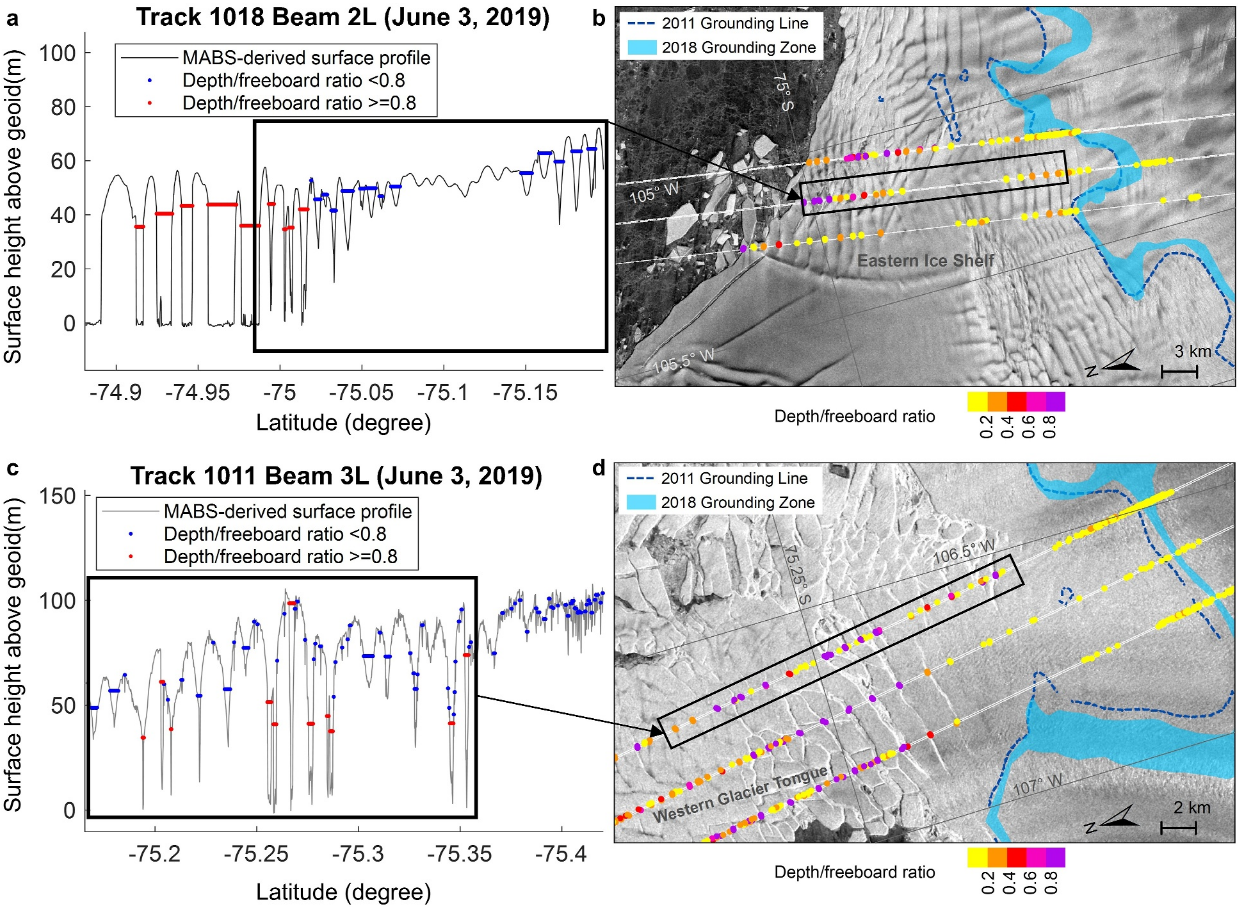

Figure 3. Illustration of fracture detection results using the improved hierarchical object-oriented method. (a, b) Fracture detection for Track 1,018 over the eastern ice shelf: (a) shows extracted fracture cross-sections from the MABS-derived surface profile (beam 2 L, strong beam) and (b) shows detected fracture center points overlaid on a Sentinel-1 image. (c, d) Same as (a, b) for Track 1,011 over the western glacier tongue. Both ICESat-2 tracks are from 3 June 2019, and the Sentinel-1 imagery is from 4 June 2019. Colors represent fracture depth/freeboard ratios. In panels (a, b), within the highlighted black box, the mean and standard deviation of fracture depth are 12.8 ± 6.9 m for the blue cross-sections (depth/freeboard ratio <0.8) and 37.6 ± 4.0 m for the red cross-sections (depth/freeboard ratio ≥0.8). In panels (c, d), the corresponding values are 16.7 ± 9.0 m for the blue cross-sections and 47.4 ± 18.5 m for the red cross-sections.

This process identifies depressions and constructs a hierarchical structure establishing the topological relationships among these features. Previously, the algorithm was successfully applied to ATL06 data over the Amery Ice Shelf (Wang et al., 2021). In this study, due to the distinct fracture morphologies between the western and eastern ice shelves, it was not feasible to apply the same filtering criteria uniformly to extract fracture features. To increase the flexibility of the algorithm in detecting different levels of surface structures, we also made several improvements: (a) Integrating additional metrics to more effectively define the morphological characteristics of fractures; (b) Applying specific filtering criteria to different types of fractures, including rifts, surface crevasses, and depressions caused by basal crevasses or channels; and (c) Refining the delineation of detected fracture features using the elbow points of the elevation profile for more accurate edge detection. Further details on these algorithm improvements are provided in the Supplement (Text S2 in Supporting Information S1).

Figure 3 presents two examples of the fracture detection results: Track 1,018 (Figures 3a and 3b) over the eastern ice shelf and Track 1,011 (Figures 3c and 3d) over the western glacier tongue, both acquired on 3 June 2019. Fracture depth was calculated as the difference in elevation between the fracture edges and the lowest point in the cross-section. For rifts, this depth represents the local freeboard height minus any mélange elevation present between the rift walls. However, multiple factors can influence this depth metric, such as ice thickness, surface variability due to snow accumulation and melt, and fracture wall morphology. To minimize the impact of these factors, we normalized the fracture depth by the freeboard height, which is calculated as the height above the geoid of the ice at the fracture edges. Using this metric, rift features exhibit high ratio values, ideally near 1 in the absence of thick mélange between rift walls. Practically, a ratio of ≥0.8 is more suitable for our study, accounting for mélange presence and dynamic ocean topography. This threshold was determined through trial-and-error experiments with various values and validated by comparisons with satellite imagery. For instance, for a rift opening at a location with an ice thickness of 400 m, the expected rift depth measured by ICESat-2 is approximately 40 m in the absence of mélange, corresponding to a depth/freeboard ratio of 1. A threshold of 0.8 allows for the presence of mélange up to 80 m thick (freeboard of 8 m). Such an assumption is reasonable given reported polar mélange thicknesses, including 34–119 m in Greenland (Meng et al., 2025) and 20 m or 52 m in a Thwaites modeling study (Crawford et al., 2024). Despite potential uncertainties introduced by mélange, it is important to note that rift detection in our algorithm also relies on other criteria (see Text S2 in Supporting Information S1). Additionally, this ratio metric can approximate the structural damage caused by basal crevasses with a surface expression (e.g., McGrath et al., 2012). In an isothermal and hydrostatic case (Coffey et al., 2024), the depth/freeboard ratio of a surface depression caused by a basal crevasse equals the total depth-to-thickness ratio, where total depth is the sum of the surface depression depth and basal crevasse height (see details in Text S3 in Supporting Information S1). Although this condition may not always be satisfied, the depth/freeboard ratio remains more effective at capturing the damage from basal crevasses than direct depth measurements.

Figures 3a and 3c show individual fracture cross-sections extracted from the MABS profile, illustrating a range of fracture types. These include large rifts with complex mélange structures between the rift walls and smaller, shallower V- or parabolic-shaped fractures. The corresponding maps (Figures 3b and 3d) display the center points and depth/freeboard ratio of each fracture cross-section. A comparison with nearly simultaneous Sentinel-1 SAR imagery shows a good match between the ICESat-2-derived fracture locations and those visible in the satellite imagery. Smaller fractures, which may be less discernible in SAR imagery due to resolution and speckle noise, are also captured by ICESat-2. Based on the shapes of surface trough profiles, the algorithm can potentially identify basal crevasse locations. A shape parameter, defined as the ratio between the width at 3/4 depth and at 1/4 depth, ranging from 1.4 to 2.8, is used to identify parabolic troughs associated with basal fractures. Most features with a depth/freeboard ratio below 0.8 in Track 1,018, over the eastern ice shelf, are likely surface troughs originating from basal crevasses. A preliminary comparison with IceBridge MCoRDS airborne radar data (Paden et al., 2010, 2014) showed good agreement between the identified basal crevasses and radar echograms (see Figure S2 and Text S4 in Supporting Information S1). It should be noted that rift features detected by the algorithm may include gaps between individual icebergs (e.g., the cross-sections marked in red in Figure 3a beyond the black box), as these gaps exhibit similar characteristics to rifts, such as high depth/freeboard ratios and U-shaped cross-sections. Overall, the evaluation shows that high-resolution ICESat-2 data, combined with our fracture detection workflow, enables detailed retrieval of vertical fracture structures, even on rapidly changing ice shelves with complex surface features.

4. Ice Flow and Fracture Characteristics of Thwaites Ice Shelf (2018–2024)

4.1. Fracture Variability From ICESat-2 Photon Heights

Using ICESat-2 photon height data, we constructed a 6-year data set of fracture vertical measurements spanning November 2018 to April 2024. The dense along-track sampling of ICESat-2 enables detailed characterization of fracture structures along each ground track, but gaps across tracks create an irregular spatial distribution of fracture measurements over time. To address this, we aggregated the depth/freeboard ratios of fractures onto a 2-km grid at annual intervals, using the center point of each fracture cross-section to represent its location. For each grid cell, we calculated the mean and maximum depth/freeboard ratios for each year (September to August), producing annual grids that effectively capture fracture patterns. However, some gaps remain due to ICESat-2 data coverage and fracture distribution.

Figure 4a presents a 2-km grid of fracture depth/freeboard ratios averaged over 6 years, providing a view of fracture distribution across the region. High ratios indicate areas where the ice column is heavily fractured. These areas include the frontal zone of the eastern ice shelf, where major rifts are consistently present, and the transitional area between the two ice shelves, with a mix of icebergs and sea ice. Most of the western glacier tongue also has high ratios, especially downstream of the 1996 grounding line. Other high-ratio areas include the shear zone between the eastern ice shelf and northern ice rises, and the section of the eastern ice shelf near the grounding line. The ratios are uniformly lower (below 0.2) upstream of the grounding zone, since detected fractures in these grounded regions are mostly shallow surface fractures with smaller widths and V-shaped profiles. Once the ice

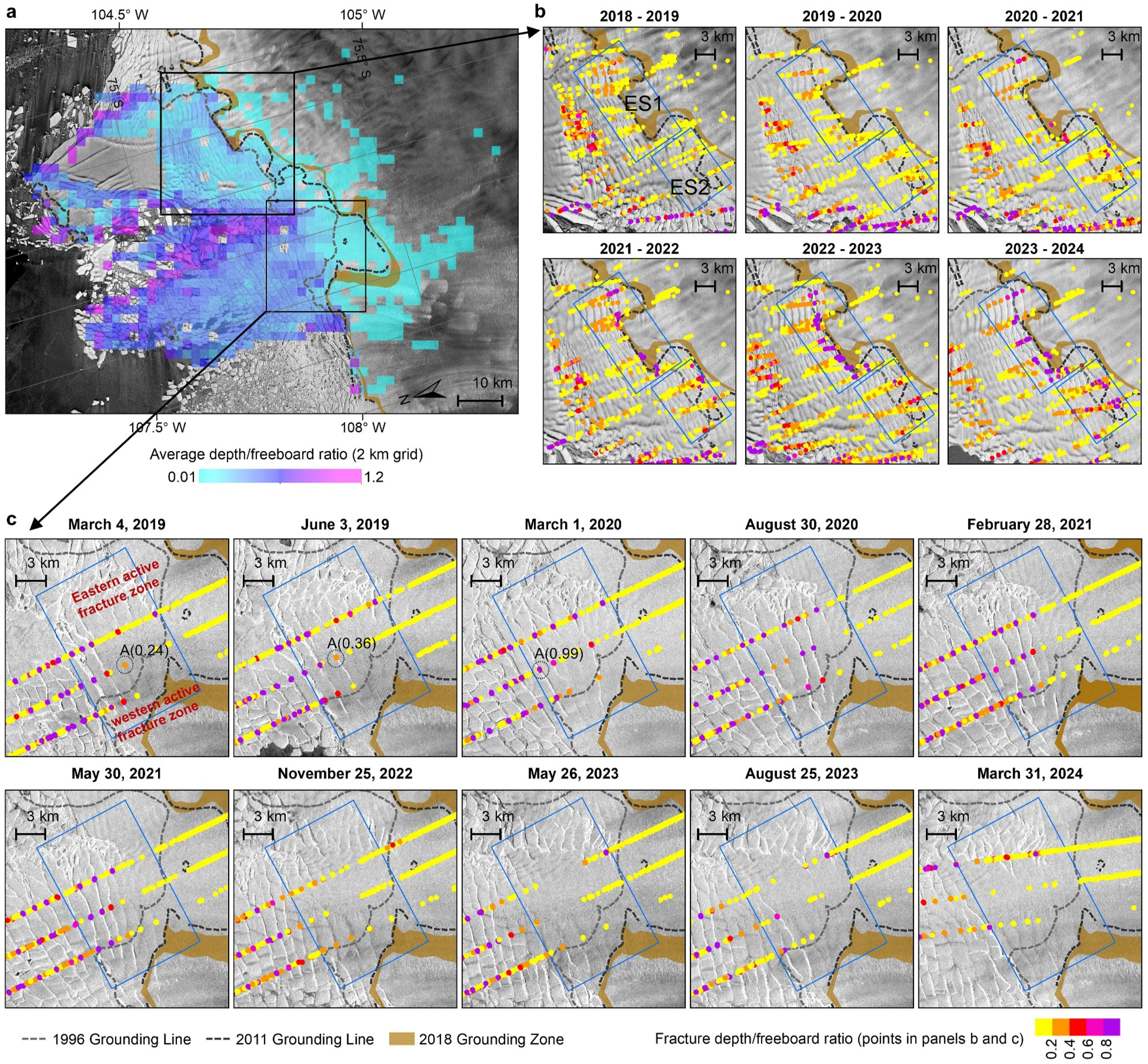

Figure 4. (a) Spatial pattern of average depth/freeboard ratios, aggregated over 6 years into a 2-km grid, with two black boxes indicating the areas shown in panels (b, c). (b) Fracture locations (center points of fracture cross-sections extracted from ICESat-2 data) on the eastern ice shelf at annual intervals (September to August), with highlighted areas showing active rift formation. (c) A selected time series of fracture locations in the active rifting zone upstream of the western glacier tongue. The dates correspond to ICESat-2 data acquisition, with nearly coincident Sentinel-1 images overlaid. The fracture locations of panels (b, c) are colored by the depth/freeboard ratio. In panel (c), fracture feature A is highlighted with depth/freeboard ratio values at three different dates to illustrate the rift formation process in this region.

becomes afloat, the ratios are mainly influenced by rifts and surface troughs caused by basal crevasses. The consistency between this ratio grid and observed structural damage suggests that the depth/freeboard ratio is an effective quantitative indicator of fracture-related damage in the Thwaites region.

Figures 4b and 4c illustrate the evolution of fractures in two key regions. Figure 4b focuses on the eastern ice shelf near the grounding zone, where fracture locations and depth/freeboard ratios are aggregated annually due to slower ice flow. The grounding line in this region is retreating, as evidenced by changes in the location of the grounding line over time. Figure 4b reveals a notable increase in fracture depth/freeboard ratios over the study period, particularly in rift formation, beginning in 2021. In the first 2 years (2018–2019 and 2019–2020), the ratios in upstream areas (marked as ES1 and ES2) remained low, barely exceeding 0.4. However, in 2020–2021, the ratios began to rise, especially near the 1996 grounding line location. By 2021–2022, the ratios in this area had significantly increased, with some values exceeding 0.8, indicating deepening fractures and active rift formation.

In 2022–2023, rift openings became more pronounced in the ES1 region, and soon afterward, they were also evident in the ES2 region.

Figure 4c presents a time series of fracture locations and depth/freeboard ratios, primarily from Track 1,011, in the active rift formation zone of the faster-moving western glacier tongue downstream of the 1996 grounding line. This area experienced significant grounding line retreat from 1996 to 2011. The most recent grounding zone (based on 2018 data), located downstream of a high rock sill (K. E. Alley et al., 2021, 2022; R. B. Alley et al., 2021, 2022), features a looping geometry that wraps around close to the 1996 grounding line. Nearly coincident Sentinel-1 images show a strong match between ICESat-2-derived fracture locations and visible fracture features, with high depth/freeboard ratios aligning well with rifts in the imagery. The time series reveals a cyclic process of rift formation, illustrated by point A in Figure 4c. On 4 March 2019, feature A had a depth/freeboard ratio of 0.24, appearing as a surface depression in ICESat-2 data—typical of basal crevasses—but not readily visible in imagery. As the ice flowed downstream, the depth/freeboard ratio increased to 0.36 by 3 June 2019, and further to 0.99 by 1 March 2020, at which point the rift was clearly visible in satellite imagery. Rifts initiated in two key zones: the eastern active fracture zone (a shear zone between the western and eastern ice shelves) and the western active fracture zone (between the 1996 and 2011 grounding lines), where the ice stretches longitudinally as it transitions from a confined to an unconfined state. Once initiated, rifts propagated rapidly about 15 km downstream of the 2011 grounding line and moved downstream, leading to the heavily crevassed surface observed across much of the western glacier tongue. Between 2019 and 2021, large transverse rifts frequently formed in the highlighted area (Figure 4c), developing from the eastern active fracture zone and propagating westward. As the highly fractured portion of the eastern zone moved downstream, the highlighted area became less fractured by 2022, and rift openings shifted further downstream. From 2022 to 2024, only one major rift formed in the highlighted area, originating from the western fracture zone and propagating eastward. Despite this shift, fracturing in the eastern zone increased again from 2023, leading to renewed rift initiation, although these rifts have not yet propagated rapidly westward. This suggests that the fracturing intensity of the eastern fracture zone plays a key role in controlling the rift behavior of the western glacier tongue. The eastern zone also serves as a key connection point between the eastern ice shelf and the western glacier tongue. When fractures are highly concentrated in the region, the connection weakens; when fractures are less frequent, the two sections become more connected.

Figure 5 displays gridded annual maximum depth/freeboard ratio values. Due to ICESat-2 data availability, there are gaps over the western glacier tongue for 2023–2024, as the 2024 data only extend to April at the time of writing. Additionally, poor data quality caused by cloud cover contributes to these gaps. Although the maximum ratio provides less detail about the variability of fracture types within each cell, it serves as a more accurate indicator of rift occurrence. Consistent with the analysis above, Figure 5 shows a clear increase over time in rift activity close to the grounding line of the eastern ice shelf (labeled ES). Another area of enhanced rift activity is the shear zone between the eastern ice shelf and the northern ice rises (labeled EN), where rifting has significantly increased since 2020–2021. By 2023–2024, nearly the entire shear margin had rifted, resembling pre-collapse changes observed on the Larsen B Ice Shelf (Wang et al., 2023). On the western glacier tongue, despite the widespread downstream rifting, a distinct boundary separates the heavily rifted downstream section from the less rifted upstream section, where rift formation rarely crosses the location of the historical 1996 grounding line. Two key transition areas are labeled WE and WW. Rift formation in WE exhibits annual variability, reflecting the changing connection between the western glacier tongue and the eastern ice shelf. For instance, fewer rifts in the WE region during 2021–2022 suggest a stronger connection between the two ice shelves. Rift activity in the WW region exhibits less variability with a possible decrease over time.

4.2. Ice Flow Variability Over 24 Seasons (2018–2024)

The formation of fractures is closely linked to the mechanical properties of the ice shelf, making fracture-flow interactions critical to ice-shelf dynamics and structural integrity. This section provides a detailed analysis of flow velocity variability over 24 seasons in the study area and its connection to fracture changes. Figure 6 presents flow velocity maps for a selected season each year, highlighting periods of significant change, such as the retreat of the western glacier tongue (summer 2018–19) and a rapid change in the transitional ice mélange area between the western and eastern ice shelves (e.g., spring 2023, winter 2024). We generated along-flow velocity profiles for one transect in the eastern section (Figure 7a) and one in the western section (Figure 7b). Additionally, average flow velocities were calculated for eight selected regions (A–H on the map), with four over the eastern ice shelf (A–D),

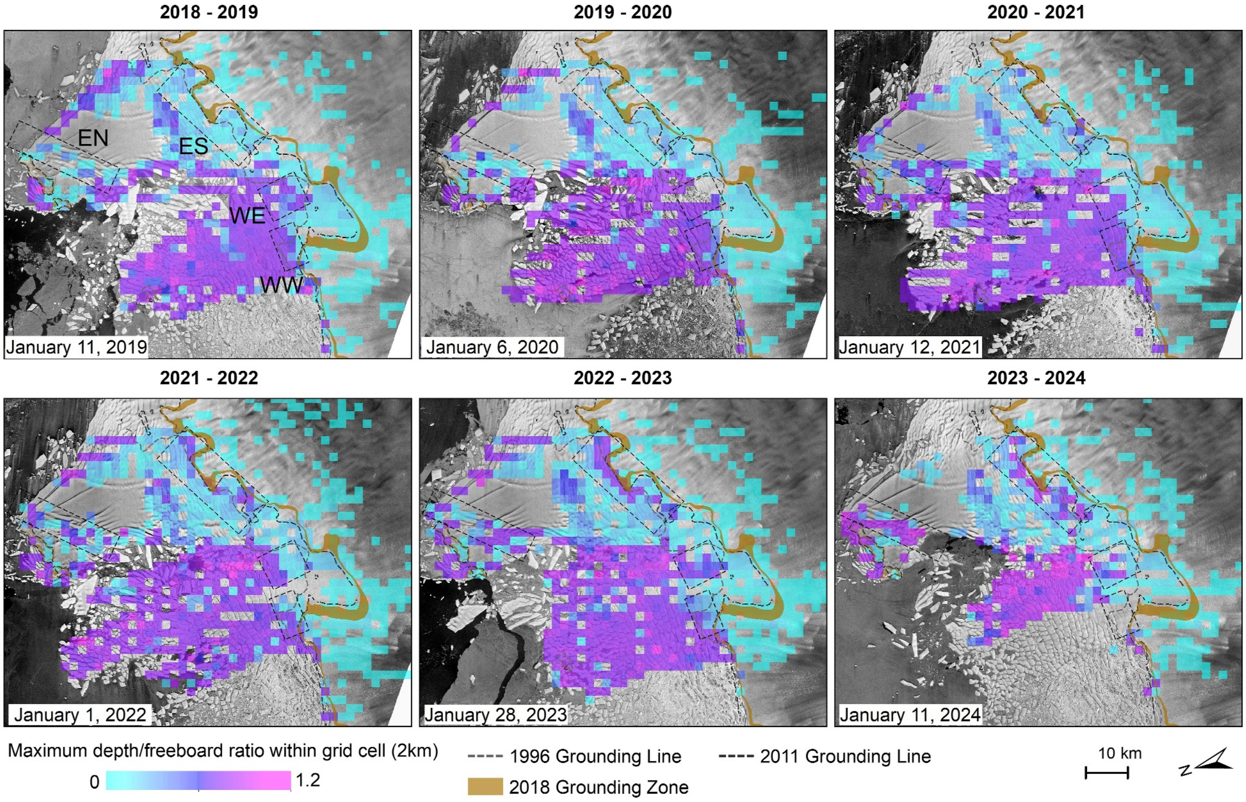

Figure 5. Annual time series of maximum fracture depth/freeboard ratio within each 2-km grid cell overlaid on selected Sentinel-1 images (acquisition dates labeled). Four areas are highlighted for discussion in the text: Eastern Ice Shelf–Northern region (EN), Eastern Ice Shelf–Southern region (ES), Western Glacier Tongue–Eastern region (WE), and Western Glacier Tongue–Western region (WW).

three covering the western glacier tongue and part of grounded ice (E–G), and one further west over the grounded ice sheet (H). Linear trends in flow velocity for these regions are shown in Figures 7c and 7d.

Spatially, the flow velocity over the western glacier tongue and across the grounding line is much higher than that of the eastern ice shelf and its grounded area (Figure 6). However, over time, these two ice shelves show nearly opposite trends (Figure 7). From 2018 to 2024, the eastern ice shelf experienced significant flow acceleration, particularly along the northwestern shear zone (Region C in Figure 6), which became more pronounced after 2021. In the shear zone, flow velocity increased by 136% from the 2018 austral spring to the winter of 2024. Other regions on the eastern ice shelf (Regions A, B, and D in Figure 6) also show persistent acceleration (Figure 7c). All regions exhibited significant linear increases in flow velocity, with the highest acceleration in the southwestern shear zone near the calving front, decreasing upstream. When comparing these flow velocity changes with fracture measurements, there is a strong correspondence between ice-shelf flow acceleration and increased fracturing near the grounding zone and along the shear zone of the eastern ice shelf (regions ES and EN of Figure 5), particularly since 2021. The acceleration of Region B (upstream of region C) in the last 2 years suggests a reduced constraining effect from the northern ice rises on the eastern ice shelf. Another notable observation is a lag in acceleration between Regions C and B: Region C (the shear zone) accelerated first, followed by Region B (middle of the ice shelf). This pattern suggests that the enhanced fracturing along the shear margin reduced the buttressing effect of the ice rises, leading to broader ice-shelf-wide accelerations.

The western glacier tongue experienced significant flow deceleration during the study period, particularly after the fall of 2020, along with reduced seasonal variability over time (Figures 7b and 7d). The velocity maps (Figure 6) show varying local flow patterns in addition to the overall slowdown, including reduced flow speeds immediately upstream of a topographic high (marked by the red dashed circle) and flow divergence around this area. In the spring of 2022, the western side of the glacier tongue exhibited anomalously high flow velocities, suggesting westward flow divergence following a calving event to the northwest. These observations highlight

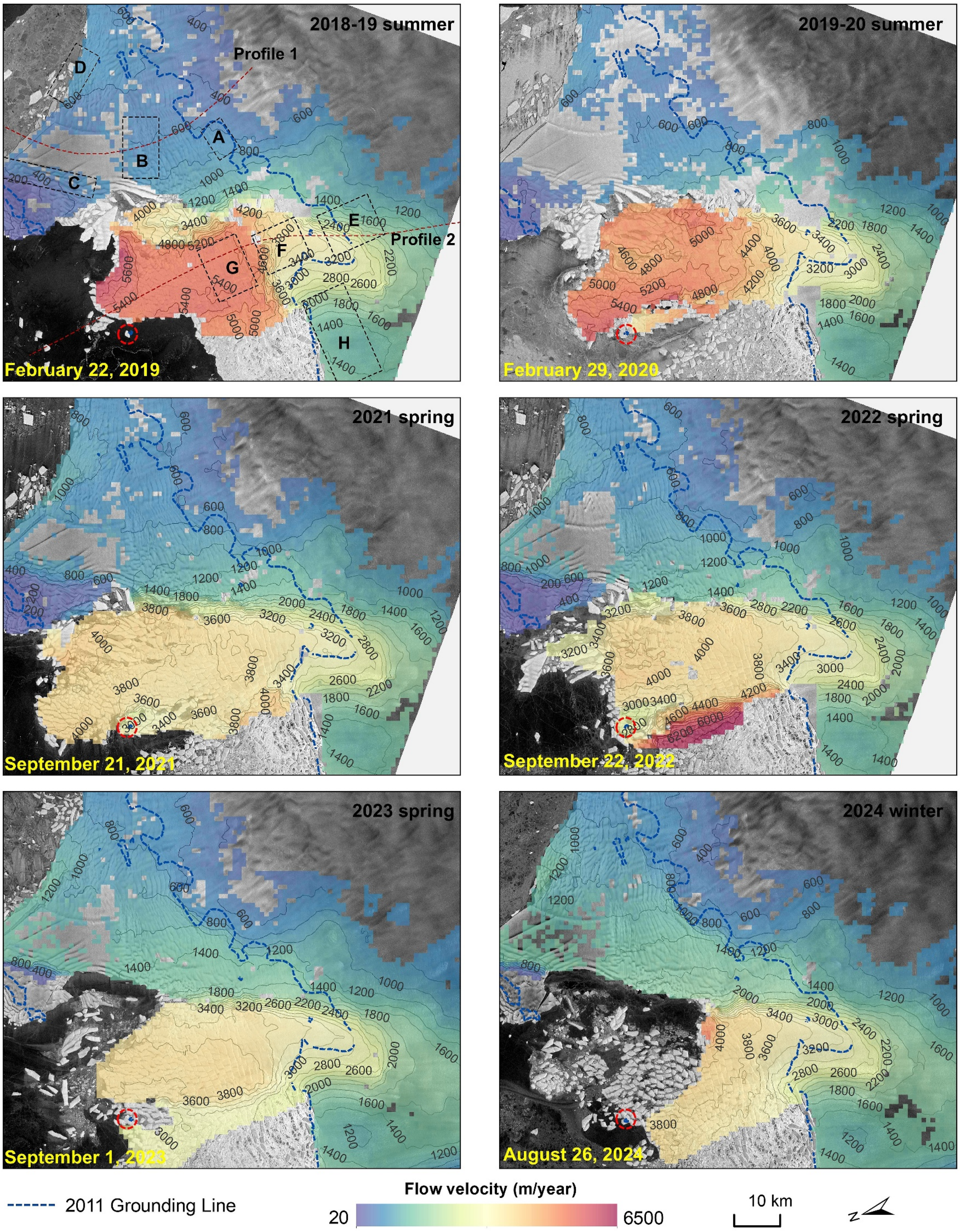

Figure 6. Flow velocity maps with velocity contours for selected seasons over the Thwaites Ice Shelf. Areas (A–H), along with two along-flow profiles (Profile 1 and Profile 2) highlighted on the 2018–19 summer velocity map, are used to generate the velocity time series shown in Figure 7. The red dashed circle highlights a local topographic high downstream of the western glacier tongue.

the critical role of this pinning point in the flow dynamics of the western glacier tongue. Although the glacier tongue has occasionally detached from the pinning point, it has reattached and experienced backstress at other times. Velocity profiles (Figure 7b) also reveal a boundary between the downstream area, where higher flow velocities and greater fluctuations (ranging from 3,500 to 6,500 m/year during 2018–2024) are observed, and the

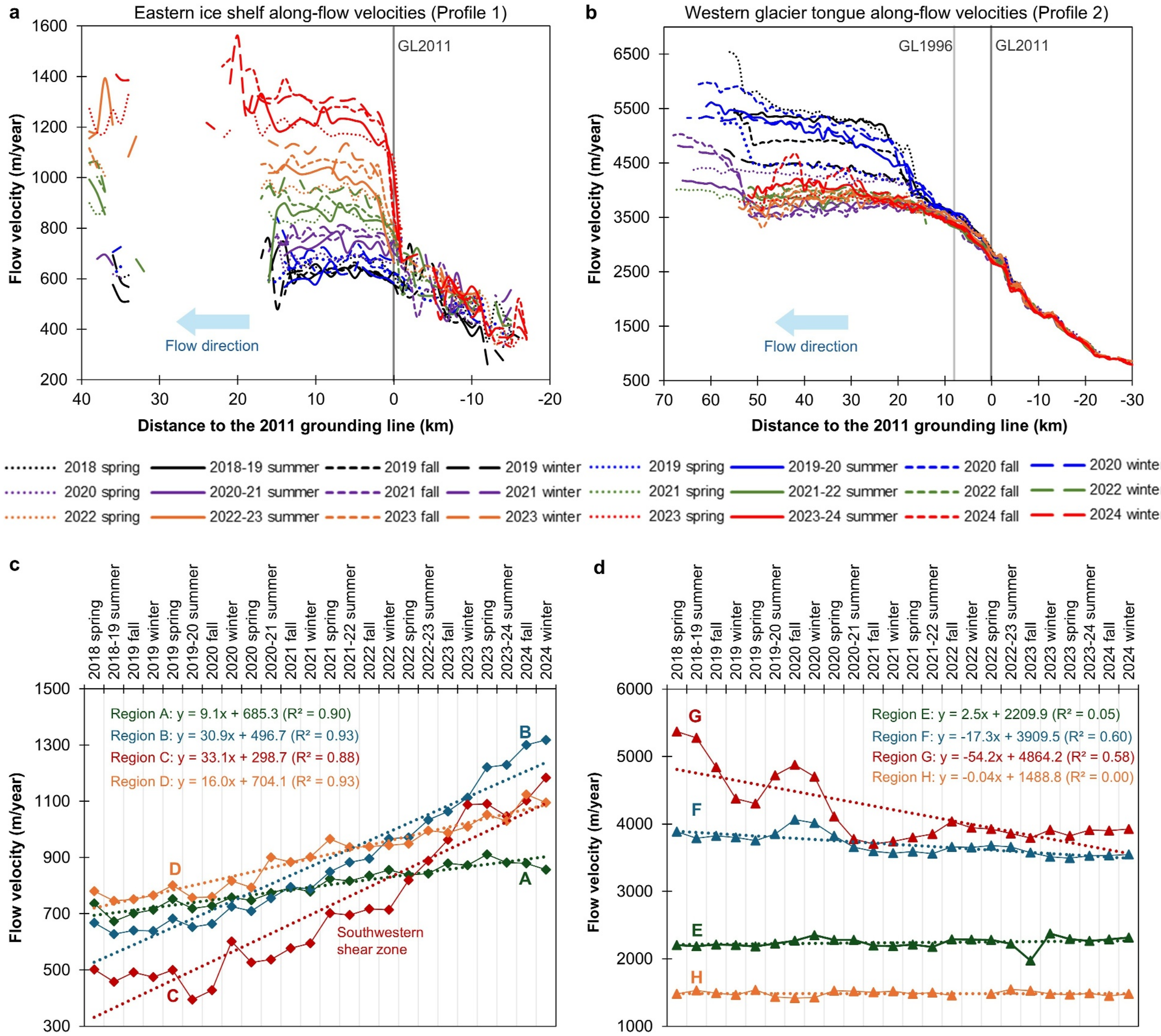

Figure 7. (a) Along-flow velocity profiles for Profile 1 across the eastern ice shelf. (b) Along-flow velocity profiles for Profile 2 along the western glacier tongue. (c) Flow velocity changes in the four regions (A–D) on the eastern ice shelf, with fitted temporal trends. (d) Flow velocity changes in the four regions (E–H) in the west, including the western glacier tongue and the further western calving front, with corresponding fitted temporal trends. Seasons here refer to austral seasons, with specific date ranges provided (Table S4 in Supporting Information S1).

upstream area, which shows much less variability. This boundary is located approximately 15 km downstream of the 2011 grounding line, coinciding with the active rift formation zone. Figure 7d presents the temporal flow velocity trends for three areas along the western glacier tongue: Region E, covering the current grounding zone; Region F, downstream of the 1996 grounding line at the active rift formation zone; and Region G, the heavily rifted western tongue downstream of the active rift formation zone. Region H, a grounded region further west and lacking ice shelf buttressing, is also shown. From 2018 to 2024, Region G exhibited a 27% velocity decrease, Region F experienced a 9% decrease, and Region E had a slight 5% increase, though with no significant trend. Region H also showed no significant change in flow velocity throughout the study period. These findings suggest that despite the significant changes in flow velocity and spatial extent of the western glacier tongue, the flow dynamics above the active rifting zone have remained relatively stable, with only minor variations. This pattern is likely due to the buttressing effect from the wrap-around geometry of the grounding zone and additional stabilization from the sill upstream of the 2018 grounding zone (Dupont & Alley, 2006; Gudmundsson et al., 2023). Furthermore, the limited influence of downstream dynamics (e.g., Region G) on upstream areas (e.g., Regions E and F) can be attributed to the largely unconfined nature of the glacier tongue downstream of the active rift formation zone. This interpretation is also supported by a recent modeling study on the two-dimensional buttressing effects in response to varying lateral conditions of ice shelves (Sergienko, 2025).

The observed deceleration of the western glacier tongue and the acceleration of the eastern ice shelf may also be driven by dynamics along the boundary connecting these two distinct ice-shelf sections. Active fracturing occurred at this boundary (the eastern active fracture zone in Figure 4c) before 2021 but became less pronounced thereafter. The flow of the eastern ice shelf is largely constrained by ice rises downstream, in contrast to the more freely floating western glacier tongue. This leads to significant differences in flow velocities between the two sections, causing high shear and active fracturing along the boundary. However, increased weakening and fracturing of the eastern ice shelf near the ice rises appears to have reduced their constraining effect, allowing the faster flow from the western glacier tongue to accelerate the eastern ice shelf. This interaction could diminish lateral shear at the boundary between the two sections, lowering the likelihood of further fracturing and reducing velocity differences between them.

4.3. Strain Rates Analysis

We further analyzed temporal changes in strain rates and explored their relationship to ICESat-2-derived fracture depth/freeboard ratios. Our objectives were to examine the mechanical behavior of ice across 24 seasons and to assess whether satellite-derived depth/freeboard ratios can effectively quantify ice-shelf structural damage related directly to ice deformation. In this analysis, we focused specifically on longitudinal strain rate and shear strain rate. Longitudinal strain rate measures the rate of ice flow speed change along the flow direction, indicating whether ice undergoes tension (positive values) or compression (negative values). Longitudinal strain rate is particularly relevant to fracture propagation and rift formation. Shear strain rate measures deformation resulting from adjacent ice parcels moving at different speeds, typically occurring in shear zones. Shear strain rates are closely linked to fracture development within these zones. Using flow velocities derived from satellite imagery, we computed these strain rates across 24 seasons, based on the equations from Bindschadler et al. (1996) and K. E. Alley et al. (2018), as detailed in Text S5 in Supporting Information S1. We adopted the "nominal" strain rate calculation method (K. E. Alley et al., 2018) using a half-length scale (r) of 1,000 m. The sign convention for shear strain rates indicates deformation direction: positive values represent right-lateral movement relative to the ice flow direction, while negative values indicate left-lateral movement. Thus, increasing positive values or decreasing negative values both signify enhanced shearing. To minimize velocity noise and align the strain rate calculations with fracture data grids, strain rates were aggregated onto a grid with 2 km resolution. Figure 8 shows the results: the spatial distribution of mean longitudinal and shear strain rates averaged over the entire study period (Figures 8a and 8b), alongside their rates of change over time (Figures 8c and 8d); the temporal evolution of longitudinal and shear strain rates in four key fracture regions (Figures 8e and 8f); and annual trends in the fracture depth/freeboard ratios averaged for these same regions (Figure 8g), as well as their relationship to the corresponding longitudinal strain rates (Figure 8h).

The average strain rate maps (Figures 8a and 8b) highlight areas of strong longitudinal extension and lateral shearing. Significant stretching occurred in the transitional zone between the western and eastern ice shelves, the grounded area above the western glacier tongue's grounding zone, the frontal area of the eastern ice shelf, and the active rift formation zone of the western glacier tongue. Strong shearing was concentrated in the northwestern shear zone of the eastern ice shelf, the transition between the two ice-shelf sections, and downstream of the western glacier tongue near the topographic high point.

The change rate maps and temporal trend analysis (Figures 8c–8f) show that the four key fracture zones experienced significant but differing changes in strain rates. The most pronounced changes occurred on the eastern ice shelf, with a significant increase in both longitudinal and shear strain rates. Specifically, in the area near the grounding line (ES), longitudinal stretching increased substantially (Figure 8e), with a linear trend leading to an average strain rate of 0.063 year^{-1} by winter 2024—nearly four times the rate in spring 2018, far exceeding fracture opening threshold values, which are typically between 0.004 year^{-1} and 0.01 year^{-1} (e.g., Rankl et al., 2017). Although shear strain rates also showed a linear increase, they were much smaller in magnitude, indicating that this region primarily experienced longitudinal stretching, contributing to the observed fracture deepening and rifting activity. In the northwestern shear zone (EN), there was a dramatic increase in the shear strain rate (Figure 8f), reaching $-0.09\ \text{year}^{-1}$, a 14.6-fold increase. This high shear is consistent with observed fracturing, and recent images (Figure S3 in Supporting Information S1) clearly show the eastern ice shelf

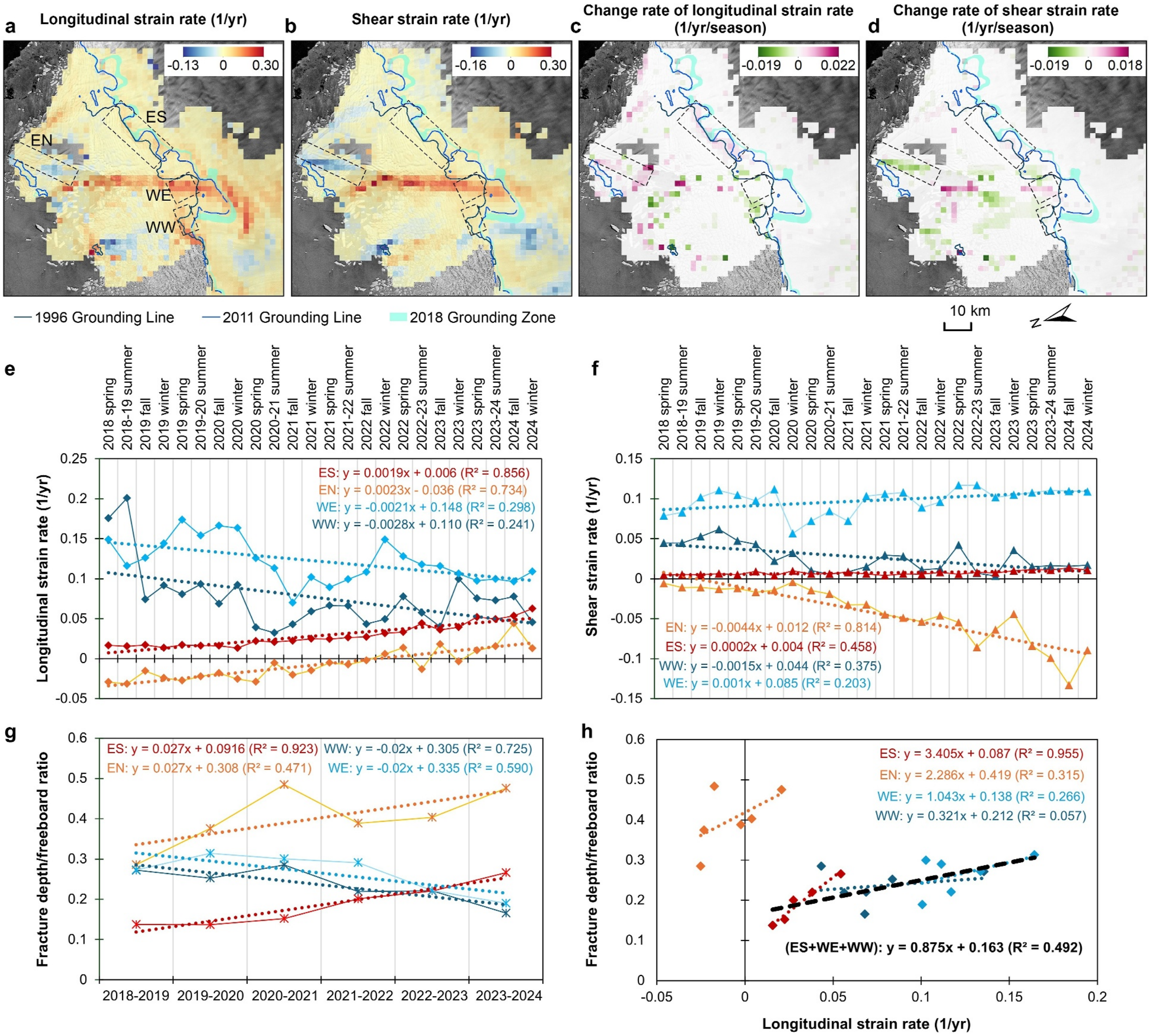

Figure 8. (a–d). Spatial patterns of strain rates and their rates of change: (a) average longitudinal strain rate, (b) average shear strain rate, (c) inter-seasonal change rate of longitudinal strain rate, and (d) inter-seasonal change rate of shear strain rate. These variables are calculated using valid strain rate data from 24 seasons based on our velocity measurements, with grid cells having valid data for more than five seasons. The change rates for grid cells with a Pearson R value below 0.5 are set to 0. (e, f). Seasonal variations in panel (e) average longitudinal and (f) shear strain rates within four regions (WE, WW, ES, EN) whose spatial extents are shown in panel (a). (g) Annual variations in average fracture depth/freeboard ratios. (h) Relationship between fracture depth/freeboard ratio and longitudinal strain rate. Best linear fits, corresponding regression equations, and R^2 values are also displayed in panels (e–h).

beginning to peel away from the fractured shear zone after the ice mélange disappeared. Beyond shear, there was also a shift in longitudinal strain rates (Figure 8e). Before winter 2022, the shear zone was dominated by longitudinal compression due to buttressing from the northern ice rises. However, after winter 2022, the zone began experiencing extensional stretching, suggesting reduced buttressing from the ice rises. A closer look at the strain rate changes in both EN and ES reveals a possible lag between the two portions: increased longitudinal stretching near the grounding line (ES) followed the changes in EN, suggesting that enhanced shear and reduced buttressing from the ice rises triggered increased fracturing near the grounding line. These strain rate changes closely align with the increasing trend of fracture depth/freeboard ratios, particularly in the ES region, which exhibits a significant linear increase over the 6-year period (Figure 8g). In the western glacier tongue zones (WW and WE), both highlighted regions exhibit a decreasing trend in fracture depth/freeboard ratios. In WW, both longitudinal and shear strain rates show a decreasing trend, which may be linked to interactions between the ice flow and the topographic high. In WE, the overall longitudinal strain rate decreased, while the shear strain rate increased slightly, though the trend was less pronounced.

Beyond the general consistency in the temporal variation trends of strain rates and depth/freeboard ratios, we further analyzed their correlations. Since depth/freeboard ratios are calculated annually, we aggregated both longitudinal and shear strain rates to an annual resolution. Although the 6-year data set may not be statistically robust enough to confirm a significant correlation, the scatter plots (Figure 8h) indicate positive correlations between longitudinal strain rates and depth/freeboard ratios in each region (EN, ES, WE, and WW). Additionally, when data from ES, WE, and WW were combined, we observed a good correlation ($R^2 = 0.492$) between longitudinal strain rates and depth/freeboard ratios. These regions are located closer to the grounding line, where longitudinal stretching plays a more dominant role in fracture development. While the EN region also shows a positive correlation, its linear relationship deviates significantly from the other three regions. This deviation is likely because fracture development in EN is primarily influenced by its high shear strain rate (Figure S4 in Supporting Information S1), which also exhibits a positive correlation with depth/freeboard ratios. These differences highlight the varying dominant roles of longitudinal stretching and lateral shear in fracture development across different regions. The good correlations between fracture depth/freeboard ratios and strain rates (Figure 8h, Figure S4 in Supporting Information S1) suggest that this satellite-derived ratio metric can serve as a valuable quantitative parameter for linking observed fracture distributions to the ice-shelf mechanical conditions. It is important to note that establishing a causal relationship between fracture development and strain rate changes requires more advanced fracture and ice flow modeling. However, most fracture modeling studies (e.g., Bassis & Ma, 2015; Coffey et al., 2024; Cook et al., 2018; Krug et al., 2014; Sun et al., 2017) remain highly idealized and often lack integration with realistic fracture data. The strong correlations observed between fracture depth/freeboard ratios and strain rates indicate the potential of using these ratio indices from satellite data to improve fracture and ice flow modeling in future research.

5. Potential Linkages to Atmospheric and Oceanic Conditions

In this section, we examine atmospheric and oceanic conditions in the Thwaites region from 2018 to 2024 using reanalysis data sets, exploring potential linkages between ice-shelf fracturing, flow behavior, and atmospheric and oceanic anomalies. We intend for this section to provide additional evidence supporting existing hypotheses and to inspire new insights into these complex interactions. We recognize that this analysis is exploratory, and fully understanding the processes by which atmospheric and oceanic conditions influence fracturing and flow dynamics requires further dedicated research.

Studies on the impact of climate forcing on ice shelf stability in the Amundsen Sea Sector have primarily focused on the intrusion of warm CDW beneath ice shelves (e.g., R. B. Alley et al., 2015; Dutrieux et al., 2014; Jacobs et al., 1996; Kimura et al., 2017; Naughten et al., 2023; Wåhlin et al., 2021; Walker et al., 2007), which enhances basal melt and weakens their structural integrity. Mechanisms by which warm ocean water destabilizes ice shelves include (e.g.,) undercutting basal channels (e.g., K. E. Alley et al., 2016, 2019, 2022a; R. B. Alley et al., 2022b; Dow et al., 2018), which can promote the formation and deepening of surface and basal fractures at channel apices, and influence the penetration depth and stability of existing fractures (e.g., Bassis & Ma, 2015; Watkins et al., 2024). However, basal melt exhibits significant spatial heterogeneity (K. E. Alley et al., 2022a; R. B. Alley et al., 2022b; Schmidt et al., 2023; Watkins et al., 2021), which is further complicated by the complex morphology of the ice shelf base, including basal channels, fractures, and overall roughness, as well as time-varying forcing from the ice sheet (Gourmelen et al., 2025). Beyond thermodynamic effects, mechanical forces may also play a key role in ice shelf weakening. Ocean wave energy can impose flexural strains on ice shelves (Lipovsky, 2018), facilitating fracture propagation, particularly when sea ice coverage is low, as sea ice acts as a natural buffer against wave-induced stress (e.g., Massom et al., 2018). Additionally, short-term processes such as hydrodynamically controlled brittle fracturing during rift propagation (Olinger et al., 2024) can also contribute to structural weakening. Understanding these processes across different timescales is highly complex and beyond the scope of this study. Here we examine anomalies in atmospheric variables, sea ice concentration, and ocean temperature and salinity at various depths to explore how large-scale atmosphere-sea-ice-ocean interactions may be broadly linked to ice shelf flow and fracturing.

Our discussion focuses on the 2018–2024 period, during which we observed increased fracturing and accelerated flow on the eastern ice shelf, in contrast to reduced fracturing and decelerated flow on the western glacier tongue.

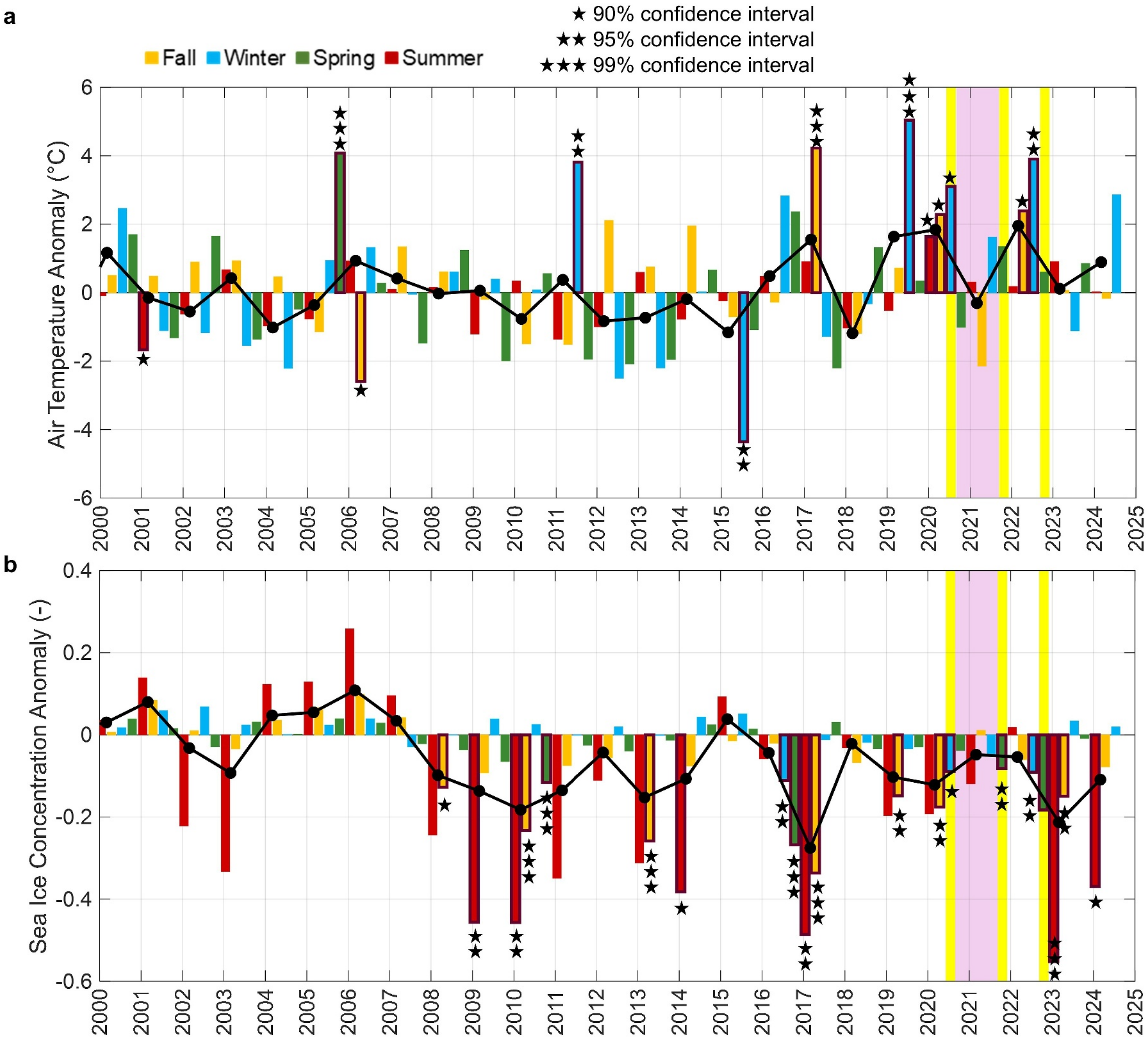

Figure 9. Time series of seasonal anomalies for (a) 2 m air temperature and (b) sea ice concentration from ERA5 over the Thwaites region (red boxed area in Figure 10). Anomalies are calculated relative to the 1979–2010 baseline period, with colors representing different seasons. The black line denotes annual average anomalies (September–August). Stars indicate anomalies that are statistically significant at the 90%, 95%, or 99% confidence intervals, based on Z-scores comparing anomalies to the mean and standard deviation of the baseline period. Seasons of flow acceleration for the eastern ice shelf are highlighted in yellow, and the onset year of increased fracture depth/freeboard ratios is highlighted in pink.

We use the 1979–2010 period as a climatological baseline for anomaly calculations and examine anomalies beginning in 2000 to provide the historical context. We note that ocean reanalysis data do not provide estimates of ocean properties beneath ice shelves, and our interpretation of ocean influences relies on reanalysis data from adjacent open water regions. Figure 9 presents seasonal and annual anomaly time series for air temperature and sea ice concentration. Anomalies were evaluated for statistical significance at the 90%, 95%, and 99% confidence levels using Z-scores. Air temperature anomalies indicate notably warm atmospheric conditions in the Thwaites region from 2019 to 2022, particularly during winter months (June–July–August, JJA). The winters of 2019, 2020, and 2022 showed significant positive deviations, with winter 2019 recording the highest air temperature anomaly (~5°C above the 1979–2010 mean). Wind data (Figures S6 and S7 in Supporting Information S1) indicate strengthened northerly winds during the warm winters of 2019 and 2020, conditions known to suppress sea ice formation. These warm atmospheric conditions correspond with observed reductions in sea ice concentration (Figure 9b), where significant negative anomalies have persisted since around 2008, most prominently in summer and fall. Recently, negative sea ice anomalies have also become more frequent during winter, with significant anomalies recorded in 2016, 2020, and 2022. Comparing these atmospheric anomalies with observed flow and fracture patterns, we found a good correspondence between increased flow velocities on the eastern ice shelf and periods of warm winter temperatures. Prominent ice-shelf acceleration occurred in the southwestern shear zone during winter (JJA) 2020, as well as spring (September–October–November, SON) 2021 and 2022 (Figure 7c; yellow highlighted periods in Figure 9). Both the winter of 2020 and the winter preceding spring 2022 exhibited significant warm air temperature anomalies (Figure 9a). Additionally, the fracture depth/freeboard ratio, indicative of structural damage, increased notably during 2020–2021 (Figure 8g; pink highlight in Figure 9), following pronounced atmospheric warming from winter 2019 through winter 2020.

Although warm atmospheric anomalies align closely with observed changes in ice flow and fracturing over the eastern ice shelf, atmospheric warming alone cannot fully explain the underlying mechanisms. Time series imagery examined in this study shows no evidence of extensive surface meltwater ponding during the study period, consistent with previous findings that surface melting in this region is typically short-lived and has not reached the intensities observed on the Antarctic Peninsula (e.g., Scambos et al., 2017). Therefore, hydrofracturing driven by abundant surface meltwater is unlikely to be the cause of the observed increase in fracturing. Instead, oceanic conditions, particularly the spatial and depth distribution of warm ocean water beneath the ice shelf, likely play a critical role. Specifically, atmospheric warming combined with reductions in sea ice concentration can influence ocean temperature and salinity, thereby impacting ice shelf structural integrity through thermodynamic processes at the ice-ocean interface. We examined anomalies in ocean potential temperature and salinity at different depth levels (10–200 m, 200–400 m, and 400–700 m). The deepest level (400–700 m), primarily occupied by warm, saline CDW, exhibits variability at decadal timescales (Figure S8 in Supporting Information S1), largely driven by westerly winds along the continental shelf break. Reanalysis data suggest that the Thwaites region generally experienced anomalous near-surface cooling along the coast from 2018 to 2024 (Figures 10b, 10d, and 10e, Figure S8 in Supporting Information S1), with this cooling extending to deeper layers to a lesser degree. In contrast, an area of persistently warm water anomalies occurred adjacent to the eastern ice shelf throughout all seasons, and was most pronounced during summer and fall (Figure 10b). This warm ocean anomaly coincided with significant reductions in sea ice concentration (Figure 10a). Seasonal sea ice loss during summer and fall, coupled with climatological offshore winds (Figure S6 in Supporting Information S1), may facilitate CDW upwelling, bringing warmer water closer to the ice shelf. Positive salinity anomalies in this region, particularly in fall and winter, further support this hypothesis (Figure 10c). Conversely, the area near the western glacier tongue exhibited persistent cooling and freshening throughout the same period (Figures 10b, 10c, 10e, and S8 in Supporting Information S1). These contrasting oceanic patterns align with increased fracturing and accelerated flow on the eastern ice shelf and, in contrast, decelerated flow and reduced rift activity within the active rift formation zone of the western glacier tongue.

Historical observations further support potential linkages between upper-ocean warming and ice shelf change, though interpretations remain somewhat speculative. In March 2002, the western glacier tongue experienced a major calving event with approximately 75 km of retreat (Miles et al., 2020). This event closely coincided with anomalously warm ocean temperatures at the 10–200 m depth from Fall 2002 (MAM) through Fall 2003 (MAM) (Figure 10e, blue highlight). However, due to its largely unconstrained geometry, this calving event minimally impacted upstream flow dynamics. In contrast, responses to fracturing on the eastern ice shelf differ notably, with weakening shear margins facilitating flow acceleration and initiating a positive feedback loop between fracturing and accelerated flow. Although upper-ocean warming anomalies observed during 2020–2021 were modest compared to the 2000–2010 decade, their timing closely aligns with increased fracturing on the eastern ice shelf (Figure 10d, pink highlight). This suggests that ocean warming, modulated by atmospheric warming and sea ice loss, may have contributed significantly to shear margin weakening and structural deterioration. The constrained lateral geometry of the eastern ice shelf further amplifies its sensitivity to fracture-driven weakening. When shear margins remain intact and strong, lateral constraints can mitigate external influences. Conversely, once fracturing along the shear margins exceeds a critical threshold, these constraints can make the ice shelf increasingly vulnerable to external perturbations. Therefore, detailed monitoring of fracture evolution, including timing, location, and extent, is essential for understanding ice shelf responses to changing atmospheric and oceanic conditions. Furthermore, ice shelf flow dynamics strongly depend on fracture locations and lateral boundary conditions (e.g., constrained vs. unconstrained), which together determine structural integrity. Comprehensive assessments of ice shelf stability thus require careful consideration of these geometric factors coupled with detailed atmosphere-sea-ice-ocean interactions. High-resolution modeling and in situ measurements of ocean properties and basal melting beneath ice shelves are critical for understanding how spatially heterogeneous basal melting influences fracture evolution, ice shelf behavior, and potential destabilization.

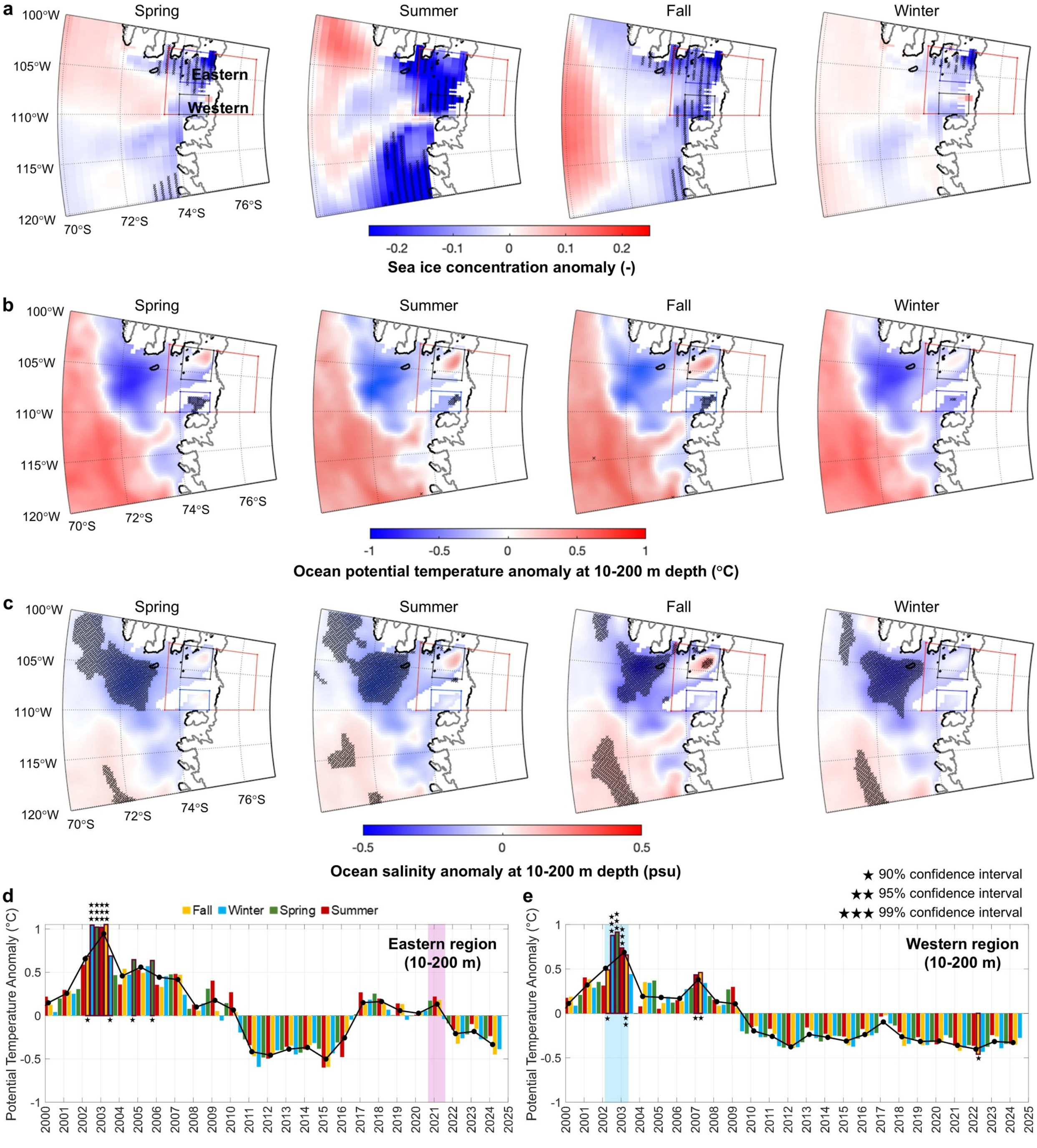

Figure 10. Average atmospheric and ocean anomalies for 2018–2024 relative to the baseline period 1979–2010. (a) Average seasonal sea ice concentration anomalies. (b) Average seasonal ocean potential temperature anomalies over the 10–200 m depth range. (c) Average seasonal ocean salinity anomalies over the 10–200 m depth range. (d, e). Time series (2000–2025) of seasonal ocean potential temperature anomalies over the 10–200 m depth range shown for the region adjacent to (d) the eastern ice shelf and (e) the region adjacent to the western glacier tongue. Colors represent different seasons, consistent with Figure 9. In panel (d), the onset year of increased fracture depth/freeboard ratios over the eastern ice shelf is highlighted in pink, while in panel (e), the period of significant oceanic warming associated with historical calving events over the western glacier tongue is highlighted in blue. The spatial extent of the eastern and western regions is outlined in panels (a–c), along with the region used for 2 m air temperature and sea ice concentration anomalies in Figure 9 (red boxed region). Hatching in panels (a–c) indicates pixels where anomalies are statistically significant at the 90% confidence level, and the coastline and grounding line (shown in black and gray) are from Gerrish et al. (2023).

6. Conclusions and Outlook

In this study, we developed a fracture-characterization workflow using ICESat-2 ATL03 geolocated photon height data by integrating a MABS algorithm with an improved object-oriented fracture-detection method. This workflow enabled the first spatially and temporally distributed vertical measurements of fractures across the Thwaites Ice Shelf from 2018 to 2024. We introduced the fracture depth/freeboard ratio as a normalized quantitative indicator of vertical structural damage caused by fracturing. Our time series analysis revealed distinct fracturing patterns between the eastern ice shelf and the western glacier tongue.

On the eastern ice shelf, fracturing intensified along the northwestern shear zone near ice rises since 2020–2021, followed by fracture deepening and rift formation near the grounding zone from 2021 to 2022. Analysis of flow velocities, strain rates, and fracture depth/freeboard ratios reveals a positive feedback loop between fracturing and accelerated ice flow (also noted in Wild et al., 2024), similar to mechanisms observed in other rapidly retreating ice shelves, including Jakobshavn Isbrae (Joughin et al., 2008), Larsen B (Wang et al., 2023), and Pine Island (Lhermitte et al., 2020). Between 2018 and 2024, the northwestern shear zone experienced a 130% increase in flow velocity, resulting in a nearly 15-fold rise in shear strain rate. Additionally, flow acceleration across the ice shelf increased the velocity contrast between the floating ice shelf and the grounded ice upstream of the grounding zone, intensifying longitudinal stretching near the grounding zone. This led to a threefold increase in longitudinal strain rate, coinciding with increased fracturing observed in ICESat-2 and Sentinel-1 data. These progressive changes indicate ongoing structural deterioration of the ice shelf. If the buttressing effect from ice rises continues to weaken, the likelihood of rapid eastern ice shelf retreat in the near future will significantly increase.

In contrast, the western glacier tongue, though highly fractured, maintained a relatively stable active rift formation zone approximately 15 km downstream of the 2011 grounding line. This region roughly marks the transition from the unconstrained downstream glacier tongue to the partially constrained upstream section, influenced by irregular grounding zone topography. ICESat-2 data reveal that rift formation in this zone follows a sequential process where shallow surface depressions, likely associated with basal crevasses, develop upstream before advecting downstream and deepening into fully formed rifts. The frequency of rift formation appears to be influenced by the degree of fracturing within the adjacent shear zone between the eastern ice shelf and western glacier tongue, with fewer rifts forming when this shear area is less fractured. Flow fluctuations, primarily characterized by deceleration, were largely confined to the downstream unconstrained section, while the upstream section remained stable throughout the study period. This contrast highlights the critical role of lateral boundary conditions in regulating ice shelf fracture-flow interactions.

Our exploratory analysis of atmospheric and oceanic reanalysis data revealed significant atmospheric warming over the Thwaites region during the 2018–2024 period, particularly during winters, coinciding with substantial sea ice decline. Seasonal variations in flow velocity showed some correspondence with these warm winters, with high-magnitude accelerations occurring during or shortly after these periods. Ocean reanalysis data indicate a general cooling trend along the Thwaites coastline but also a persistent warm anomaly at shallower depths near the eastern ice shelf. This anomaly may affect thinner, more vulnerable areas of the ice shelf, such as basal crevasses and channels, accelerating basal melting and promoting fracture growth in high-strain regions such as the northwestern shear zone. In contrast, the western portion of Thwaites exhibits a cooling trend coincident with the observed deceleration in ice flow. Moreover, lateral boundary conditions, whether an ice shelf is confined, unconfined, or partially constrained, likely play a crucial role in modulating ice-shelf structural responses to oceanic forcing.

The Thwaites Ice Shelf case study demonstrates the robust capability of ICESat-2 in quantifying fracture-induced vertical structural damage and its evolution, and the value of continuing such measurements. The workflow developed in this study provides a foundation for future pan-Antarctic fracture assessments. The fracture depth/freeboard ratio shows promise as a quantitative metric for incorporating fracture-induced vertical damage into numerical models of ice fracturing and flow, enabling more realistic representations of fracture evolution rather than relying solely on theoretical assumptions. Nevertheless, ICESat-2's across-track data gaps and its 91-day revisit period pose limitations for monitoring rapid fracture evolution. High-resolution fracture measurements are important for calibrating and improving models of fracturing and calving processes, a fundamental step in reducing uncertainties in projections of Antarctic ice loss. Future satellite altimetry missions with even higher spatial and temporal resolutions, such as the planned Earth Dynamics Geodetic Explorer mission (Fricker et al., 2025), would be instrumental for capturing these dynamic processes with greater precision. Furthermore, understanding the complex interactions between atmosphere, sea ice, ocean conditions, and ice shelf basal processes requires high-resolution ice-ocean modeling, improved observations beneath the ice shelf, and enhanced characterization of basal morphology and its temporal evolution. Future research should also integrate high-resolution observational data with numerical modeling to improve both the understanding and predictive capabilities of the mechanisms driving ice shelf weakening and retreat.

Data Availability Statement

The derived data sets (Wang et al., 2024), including fracture depth/freeboard ratio grids, flow velocities, and strain rates, can be accessed from https://doi.org/10.6084/m9.figshare.27129105.v2. There are no restrictions on accessing the original data used in this study. The ICESat-2 ATL03 geolocated photon data product (Neumann et al., 2021, 2023) and ATL06 land ice height data product (Smith et al., 2021, 2023) were accessed from the National Snow and Ice Data Center. The Landsat-8 OLI (EROS Center, 2017) images were downloaded from the USGS EarthExplorer data portal, courtesy of the U.S. Geological Survey. Copernicus Sentinel-1 data (2018–2024) (Torres et al., 2017) were retrieved from ASF DAAC (https://www.earthdata.nasa.gov/data/platforms/space-based-platforms/sentinel-1) (1 September 2024), processed by ESA. The ECMWF Reanalysis fifth Generation (ERA5) (Hersbach et al., 2023) and the ECMWF ORAS5 (Copernicus Climate Change Service, Climate Data Store, 2021) were retrieved from the Copernicus Climate Change Service (C3S) Climate Data Store.

Acknowledgments

The authors acknowledge support from the NASA Cryospheric Sciences Program 80NSSC22K0384 (SW, RBA, ZH), the U.S. National Science Foundation NSF-NERC-OPP-1738934 (SA, RBA, BRP, AGW), the Heising-Simons Foundation under Grant 2018-0769 (SA, BRP, RBA), the NASA 21-EARTH21-0243 (SA, AGW, RBA), and the Penn State College of Earth and Mineral Sciences John T. Ryan, Jr. Faculty Fellowship (SW). The authors acknowledge the National Snow and Ice Data Center for ICESat-2 ATL03 and ATL06 data, the United States Geological Survey (USGS) for the Landsat images, the European Space Agency for the Sentinel-1 SAR images and SNAP software, and the European Centre for Medium-Range Weather Forecasts (ECMWF) for the ORAS5 and ERA-5 reanalysis data. We also thank the editors and four anonymous reviewers for their constructive comments and suggestions that greatly improved the manuscript.

References

Alley, K. E., Scambos, T. A., & Alley, R. B. (2022). The role of channelized basal melt in ice-shelf stability: Recent progress and future priorities. *Annals of Glaciology*, *63*(87–89), 18–22. https://doi.org/10.1017/aog.2023.5

Alley, K. E., Scambos, T. A., Alley, R. B., & Holschuh, N. (2019). Troughs developed in ice-stream shear margins precondition ice shelves for ocean-driven breakup. *Science Advances*, *5*(10), eaax2215. https://doi.org/10.1126/sciadv.aax2215

Alley, K. E., Scambos, T. A., Anderson, R. S., Rajaram, H., Pope, A., & Haran, T. M. (2018). Continent-wide estimates of Antarctic strain rates from Landsat 8-derived velocity grids. *Journal of Glaciology*, *64*(244), 321–332. https://doi.org/10.1017/jog.2018.23

Alley, K. E., Scambos, T. A., Siegfried, M. R., & Fricker, H. A. (2016). Impacts of warm water on Antarctic ice shelf stability through basal channel formation. *Nature Geoscience*, *9*(4), 290–293. https://doi.org/10.1038/ngeo2675

Alley, K. E., Wild, C. T., Luckman, A., Scambos, T. A., Truffer, M., Pettit, E. C., et al. (2021). Two decades of dynamic change and progressive destabilization on the Thwaites Eastern Ice Shelf. *The Cryosphere*, *15*(11), 5187–5203. https://doi.org/10.5194/tc-15-5187-2021

Alley, R. B., Anandakrishnan, S., Christianson, K., Horgan, H. J., Muto, A., Parizek, B. R., et al. (2015). Oceanic forcing of ice-sheet retreat: West Antarctica and more. *Annual Review of Earth and Planetary Sciences*, *43*(1), 207–231. https://doi.org/10.1146/annurev-earth-060614-105344

Alley, R. B., Cuffey, K. M., Bassis, J. N., Alley, K. E., Wang, S., Parizek, B. R., et al. (2023). Iceberg calving: Regimes and transitions. *Annual Review of Earth and Planetary Sciences*, *51*(1), 189–215. https://doi.org/10.1146/annurev-earth-032320-110916

Alley, R. B., Dupont, T. K., Parizek, B. R., & Anandakrishnan, S. (2005). Access of surface meltwater to beds of sub-freezing glaciers: Preliminary insights. *Annals of Glaciology*, *40*, 8–14. https://doi.org/10.3189/172756405781813483

Alley, R. B., Holschuh, N., MacAyeal, D. R., Parizek, B. R., Zoet, L., Riverman, K., et al. (2021). Bedforms of Thwaites Glacier, West Antarctica: Character and origin. *Journal of Geophysical Research: Earth Surface*, *126*(12). https://doi.org/10.1029/2021jf006339

Alley, R. B., Holschuh, N., Parizek, B., Zoet, L. K., Riverman, K., Muto, A., et al. (2022). Ghostly flute music: Drumlins, moats and the bed of Thwaites Glacier. *Annals of Glaciology*, *63*(87–89), 153–157. https://doi.org/10.1017/aog.2023.43

Andreasen, J. R., Hogg, A. E., & Selley, H. L. (2023). Change in Antarctic ice shelf area from 2009 to 2019. *The Cryosphere*, *17*(5), 2059–2072. https://doi.org/10.5194/tc-17-2059-2023

Banwell, A. F., MacAyeal, D. R., & Sergienko, O. V. (2013). Breakup of the Larsen B Ice Shelf triggered by chain reaction drainage of supraglacial lakes. *Geophysical Research Letters*, *40*(22), 5872–5876. https://doi.org/10.1002/2013gl057694

Bassis, J. N., Crawford, A., Kachuck, S. B., Benn, D. I., Walker, C., Millstein, J., et al. (2024). Stability of ice shelves and ice cliffs in a changing climate. *Annual Review of Earth and Planetary Sciences*, *52*(1), 221–247. https://doi.org/10.1146/annurev-earth-040522-122817

Bassis, J. N., & Ma, Y. (2015). Evolution of basal crevasses links ice shelf stability to ocean forcing. *Earth and Planetary Science Letters*, *409*, 203–211. https://doi.org/10.1016/j.epsl.2014.11.003

Bell, R. E., Banwell, A. F., Trusel, L. D., & Kingslake, J. (2018). Antarctic surface hydrology and impacts on ice-sheet mass balance. *Nature Climate Change*, *8*(12), 1044–1052. https://doi.org/10.1038/s41558-018-0326-3

Benn, D. I., & Åström, J. A. (2018). Calving glaciers and ice shelves. *Advances in Physics X*, *3*(1), 1513819. https://doi.org/10.1080/23746149.2018.1513819

Benn, D. I., Luckman, A., Åström, J. A., Crawford, A. J., Cornford, S. L., Bevan, S. L., et al. (2022). Rapid fragmentation of Thwaites Eastern Ice Shelf. *The Cryosphere*, *16*(6), 2545–2564. https://doi.org/10.5194/tc-16-2545-2022

Benn, D. I., Warren, C. R., & Mottram, R. H. (2007). Calving processes and the dynamics of calving glaciers. *Earth-Science Reviews*, *82*(3), 143–179. https://doi.org/10.1016/j.earscirev.2007.02.002

Bindschadler, R., Vornberger, P., Blankenship, D., Scambos, T., & Jacobel, R. (1996). Surface velocity and mass balance of ice streams D and E, west Antarctica. *Journal of Glaciology*, *42*(142), 461–475. https://doi.org/10.3189/S0022143000003452

Brenner, A. C., DiMarzio, J. P., & Jay Zwally, H. (2007). Precision and accuracy of satellite radar and laser altimeter data over the continental ice sheets. *IEEE Transactions on Geoscience and Remote Sensing*, *45*(2), 321–331. https://doi.org/10.1109/tgrs.2006.887172

Coffey, N. B., Lai, C., Wang, Y., Buck, W. R., Surawy-Stepney, T., & Hogg, A. E. (2024). Theoretical stability of ice shelf basal crevasses with a vertical temperature profile. *Journal of Glaciology*, *70*, e64. https://doi.org/10.1017/jog.2024.52

Cook, S., Åström, J., Zwinger, T., Galton-Fenzi, B. K., Greenbaum, J. S., & Coleman, R. (2018). Modelled fracture and calving on the Totten Ice Shelf. *The Cryosphere*, *12*(7), 2401–2411. https://doi.org/10.5194/tc-12-2401-2018

Copernicus Climate Change Service, Climate Data Store. (2021). ORAS5 global ocean reanalysis monthly data from 1958 to present [Dataset]. *Copernicus Climate Change Service (C3S) Climate Data Store (CDS)*. https://doi.org/10.24381/cds.67e8eeb7

Crawford, A., Åström, J., Benn, D. I., Luckman, A., Gladstone, R., Zwinger, T., et al. (2024). Calving dynamics and the potential impact of mélange buttressing at the western calving front of Thwaites Glacier, West Antarctica. *Journal of Geophysical Research: Earth Surface*, *129*(10), e2024JF007737. https://doi.org/10.1029/2024jf007737

DeConto, R. M., & Pollard, D. (2016). Contribution of Antarctica to past and future sea-level rise. *Nature*, *531*(7596), 591–597. https://doi.org/10.1038/nature17145

DeConto, R. M., Pollard, D., Alley, R. B., Velicogna, I., Gasson, E., Gomez, N., et al. (2021). The Paris climate agreement and future sea-level rise from Antarctica. *Nature*, *593*(7857), 83–89. https://doi.org/10.1038/s41586-021-03427-0

Doake, C. S. M., Corr, H. F. J., Rott, H., Skvarca, P., & Young, N. W. (1998). Breakup and conditions for stability of the Northern Larsen Ice Shelf, Antarctica. *Nature*, *391*(6669), 778–780. https://doi.org/10.1038/35832

Dow, C. F., Lee, W. S., Greenbaum, J. S., Greene, C. A., Blankenship, D. D., Poinar, K., et al. (2018). Basal channels drive active surface hydrology and Transverse ice shelf fracture. *Science Advances*, *4*(6), eaao7212. https://doi.org/10.1126/sciadv.aao7212

Dupont, T. K., & Alley, R. B. (2006). Role of small ice shelves in sea-level rise. *Geophysical Research Letters*, *33*(9). https://doi.org/10.1029/2005gl025665

Dutrieux, P., De Rydt, J., Jenkins, A., Holland, P. R., Ha, H. K., Lee, S. H., et al. (2014). Strong sensitivity of Pine Island ice-shelf melting to climatic variability. *Science*, *343*(6167), 174–178. https://doi.org/10.1126/science.1244341

Earth Resources Observation and Science (EROS) Center. (2017). Landsat 8 operational land imager/thermal infrared sensor level-1, collection 1 [Dataset]. *U.S. Geological Survey*. https://doi.org/10.5066/F71835S6

Edwards, T. L., Nowicki, S., Marzeion, B., Hock, R., Goelzer, H., Seroussi, H., et al. (2021). Projected land ice contributions to twenty-first-century sea level rise. *Nature*, *593*(7857), 74–82. https://doi.org/10.1038/s41586-021-03302-y

Fricker, H. A., Galton-Fenzi, B. K., Walker, C. C., Freer, B. I. D., Padman, L., & DeConto, R. (2025). Antarctica in 2025: Drivers of deep uncertainty in projected ice loss. *Science*, *387*(6734), 601–609. https://doi.org/10.1126/science.adt9619

Fricker, H. A., Young, N. W., Coleman, R., Bassis, J. N., & Minster, J.-B. (2005). Multi-year monitoring of rift propagation on the Amery Ice Shelf, East Antarctica. *Geophysical Research Letters*, *32*(2). https://doi.org/10.1029/2004GL021036

Gerrish, L., Ireland, L., Fretwell, P., & Cooper, P. (2023). High resolution vector polygons of the Antarctic coastline (7.8) [Dataset]. *UK Polar Data Centre, Natural Environment Research Council, UK Research & Innovation*. https://doi.org/10.5285/c7fe759d-e042-479a-9ecf-274255b4f0a1

Glasser, N. F., & Scambos, T. A. (2008). A structural glaciological analysis of the 2002 Larsen B ice-shelf collapse. *Journal of Glaciology*, *54*(184), 3–16. https://doi.org/10.3189/002214308784409017

Gourmelen, N., Jakob, L., Holland, P. R., Dutrieux, P., Goldberg, D., Bevan, S., et al. (2025). The influence of subglacial lake discharge on Thwaites Glacier ice-shelf melting and grounding-line retreat. *Nature Communications*, *16*(2272), 2272. https://doi.org/10.1038/s41467-025-57417-1

Gudmundsson, G. H., Barnes, J. M., Goldberg, D. N., & Morlighem, M. (2023). Limited impact of Thwaites Ice Shelf on future ice loss from Antarctica. *Geophysical Research Letters*, *50*(11). https://doi.org/10.1029/2023gl102880

Hersbach, H., Bell, B., Berrisford, P., Biavati, G., Horányi, A., Muñoz Sabater, J., et al. (2023). ERA5 monthly averaged data on single levels from 1940 to present [Dataset]. *Copernicus Climate Change Service (C3S) Climate Data Store (CDS)*. https://doi.org/10.24381/cds.f17050d7

Hersbach, H., Bell, B., Berrisford, P., Hirahara, S., Horányi, A., Muñoz-Sabater, J., et al. (2020). The ERA5 global reanalysis. *Quarterly Journal of the Royal Meteorological Society*, *146*(730), 1999–2049. https://doi.org/10.1002/qj.3803

Herzfeld, U. C., Trantow, T., Lawson, M., Hans, J., & Medley, G. (2021). Surface heights and crevasse morphologies of surging and fast-moving glaciers from ICESat-2 laser altimeter data - Application of the density-dimension algorithm (DDA-ice) and evaluation using airborne altimeter and Planet SkySat data. *Science of Remote Sensing*, *3*, 100013. https://doi.org/10.1016/j.srs.2020.100013

Howat, I. M., Porter, C., Smith, B. E., Noh, M.-J., & Morin, P. (2019). The reference elevation model of Antarctica. *The Cryosphere*, *13*(2), 665–674. https://doi.org/10.5194/tc-13-665-2019

Hughes, T. (1983). On the disintegration of ice shelves: The role of fracture. *Journal of Glaciology*, *29*(101), 98–117. https://doi.org/10.3189/s0022143000005177

Hulbe, C. L., LeDoux, C., & Cruikshank, K. (2010). Propagation of long fractures in the Ronne Ice Shelf, Antarctica, investigated using a numerical model of fracture propagation. *Journal of Glaciology*, *56*(197), 459–472. https://doi.org/10.3189/002214310792447743

Jacobs, S. S., Hellmer, H. H., & Jenkins, A. (1996). Antarctic ice sheet melting in the Southeast Pacific. *Geophysical Research Letters*, *23*(9), 957–960. https://doi.org/10.1029/96GL00723

Jenkins, A., Shoosmith, D., Dutrieux, P., Jacobs, S., Kim, T. W., Lee, S. H., et al. (2018). West Antarctic ice sheet retreat in the Amundsen Sea driven by decadal oceanic variability. *Nature Geoscience*, *11*(10), 733–738. https://doi.org/10.1038/s41561-018-0207-4

Joughin, I., & Alley, R. B. (2011). Stability of the West Antarctic ice sheet in a warming world. *Nature Geoscience*, *4*(8), 506–513. https://doi.org/10.1038/ngeo1194

Joughin, I., Howat, I. M., Fahnestock, M., Smith, B., Krabill, W., Alley, R. B., et al. (2008). Continued evolution of Jakobshavn Isbrae following its rapid speedup. *Journal of Geophysical Research*, *113*(F4). https://doi.org/10.1029/2008jf001023

Joughin, I., & MacAyeal, D. R. (2005). Calving of large tabular icebergs from ice shelf rift systems. *Geophysical Research Letters*, *32*(2), 195. https://doi.org/10.1029/2004gl020978

Joughin, I., Smith, B. E., & Medley, B. (2014). Marine ice sheet collapse potentially under way for the Thwaites Glacier Basin, West Antarctica. *Science*, *344*(6185), 735–738. https://doi.org/10.1126/science.1249055

Kimura, S., Jenkins, A., Regan, H., Holland, P. R., Assmann, K. M., Whitt, D. B., et al. (2017). Oceanographic controls on the variability of ice-shelf basal melting and circulation of glacial meltwater in the Amundsen Sea embayment, Antarctica. *Journal of Geophysical Research, C: Oceans*, *122*(12), 10131–10155. https://doi.org/10.1002/2017jc012926

Kopp, R. E., DeConto, R. M., Bader, D. A., Hay, C. C., Horton, R. M., Kulp, S., et al. (2017). Evolving understanding of Antarctic ice-sheet physics and ambiguity in probabilistic sea-level projections. *Earth's Future*, *5*(12), 1217–1233. https://doi.org/10.1002/2017ef000663

Krug, J., Weiss, J., Gagliardini, O., & Durand, G. (2014). Combining damage and fracture mechanics to model calving. *The Cryosphere*, *8*(6), 2101–2117. https://doi.org/10.5194/tc-8-2101-2014

Kwok, R., Cunningham, G., Markus, T., Hancock, D., Morison, J. H., Palm, S. P., et al., the ICESat-2 Science Team (2020). ATLAS/ICESat-2 L3A sea ice freeboard, version 3 [Dataset]. *National Snow and Ice Data Center*. https://doi.org/10.5067/ATLAS/ATL10.003

Lai, C.-Y., Kingslake, J., Wearing, M. G., Chen, P.-H. C., Gentine, P., Li, H., et al. (2020). Vulnerability of Antarctica's ice shelves to meltwater-driven fracture. *Nature*, *584*(7822), 574–578. https://doi.org/10.1038/s41586-020-2627-8

Lescarmontier, L., Legresy, B., Young, N. W., Coleman, R., Testut, L., Mayet, C., & Lacroix, P. (2015). Rifting processes and ice-flow modulation observed on Mertz Glacier, East Antarctica. *Journal of Glaciology*, *61*(230), 1183–1193. https://doi.org/10.3189/2015jog15j028

Lhermitte, S., Sun, S., Shuman, C., Wouters, B., Pattyn, F., Wuite, J., et al. (2020). Damage accelerates ice shelf instability and mass loss in Amundsen Sea embayment. *Proceedings of the National Academy of Sciences of the United States of America*, *117*(40), 24735–24741. https://doi.org/10.1073/pnas.1912890117

Li, G., Guo, J., Pei, L., Zhang, S., Tang, X., & Yao, J. (2021). Extraction and analysis of the three-dimensional features of crevasses in the Amery Ice Shelf based on ICESat-2 ATL06 data. *IEEE Journal of Selected Topics in Applied Earth Observations and Remote Sensing*, *14*, 5796–5806. https://doi.org/10.1109/jstars.2021.3085302

Lipovsky, B. P. (2018). Ice shelf rift propagation and the mechanics of wave-induced fracture. *Journal of Geophysical Research: Oceans*, *123*(6), 4014–4033. https://doi.org/10.1029/2017jc013664

Liu, H., Wang, L., Tang, S.-J., & Jezek, K. C. (2012). Robust multi-scale image matching for deriving ice surface velocity field from sequential satellite images. *International Journal of Remote Sensing*, *33*(6), 1799–1822. https://doi.org/10.1080/01431161.2011.602128

MacAyeal, D. R., Scambos, T. A., Hulbe, C. L., & Fahnestock, M. A. (2003). Catastrophic ice-shelf break-up by an ice-shelf-fragment-capsize mechanism. *Journal of Glaciology*, *49*(164), 22–36. https://doi.org/10.3189/172756503781830863

Markus, T., Neumann, T., Martino, A., Abdalati, W., Brunt, K., Csatho, B., et al. (2017). The ice, cloud, and land elevation satellite-2 (ICESat-2): Science requirements, concept, and implementation. *Remote Sensing of Environment*, *190*, 260–273. https://doi.org/10.1016/j.rse.2016.12.029

Massom, R. A., Scambos, T. A., Bennetts, L. G., Reid, P., Squire, V. A., & Stammerjohn, S. E. (2018). Antarctic ice shelf disintegration triggered by sea ice loss and ocean swell. *Nature*, *558*(7710), 383–389. https://doi.org/10.1038/s41586-018-0212-1

McGrath, D., Steffen, K., Rajaram, H., Scambos, T., Abdalati, W., & Rignot, E. (2012). Basal crevasses on the Larsen C ice shelf, Antarctica: Implications for meltwater ponding and hydrofracture. *Geophysical Research Letters*, *39*(16), L16504. https://doi.org/10.1029/2012gl052413

Meng, Y., Lai, C.-Y., Culberg, R., Shahin, M. G., Stearns, L. A., Burton, J. C., & Nissanka, K. (2025). Seasonal changes of mélange thickness coincide with Greenland calving dynamics. *Nature Communications*, *16*(1), 573. https://doi.org/10.1038/s41467-024-55241-7

Miles, B. W. J., Stokes, C. R., Jenkins, A., Jordan, J. R., Jamieson, S. S. R., & Gudmundsson, G. H. (2020). Intermittent structural weakening and acceleration of the Thwaites Glacier Tongue between 2000 and 2018. *Journal of Glaciology*, *66*(257), 485–495. https://doi.org/10.1017/jog.2020.20

Milillo, P., Rignot, E., Rizzoli, P., Scheuchl, B., Mouginot, J., Bueso-Bello, J., & Prats-Iraola, P. (2019). Heterogeneous retreat and ice melt of Thwaites Glacier, West Antarctica. *Science Advances*, *5*(1), eaau3433. https://doi.org/10.1126/sciadv.aau3433

Nakayama, Y., Manucharyan, G., Zhang, H., Dutrieux, P., Torres, H. S., Klein, P., et al. (2019). Pathways of ocean heat towards Pine Island and Thwaites grounding lines. *Scientific Reports*, *9*(1), 16649. https://doi.org/10.1038/s41598-019-53190-6

Narine, L., Malambo, L., & Popescu, S. (2022). Characterizing canopy cover with ICESat-2: A case study of southern forests in Texas and Alabama, USA. *Remote Sensing of Environment*, *281*, 113242. https://doi.org/10.1016/j.rse.2022.113242

Naughten, K. A., Holland, P. R., & De Rydt, J. (2023). Unavoidable future increase in West Antarctic ice-shelf melting over the twenty-first century. *Nature Climate Change*, *13*(11), 1222–1228. https://doi.org/10.1038/s41558-023-01818-x

Neumann, T. A., Brenner, A., Hancock, D., Robbins, J., Gibbons, A., Lee, J., et al. (2023). ATLAS/ICESat-2 L2A global geolocated photon data. (ATL03, version 6) [Dataset]. *NASA National Snow and Ice Data Center Distributed Active Archive Center*. https://doi.org/10.5067/ATLAS/ATL03.006

Neumann, T. A., Brenner, A., Hancock, D., Robbins, J., Saba, J., Harbeck, K., et al. (2021). ATLAS/ICESat-2 L2A global geolocated photon data, version 5 [Dataset]. *NASA National Snow and Ice Data Center Distributed Active Archive Center*. https://doi.org/10.5067/ATLAS/ATL03.005

Neumann, T. A., Martino, A. J., Markus, T., Bae, S., Bock, M. R., Brenner, A. C., et al. (2019). The ice, cloud, and land elevation satellite - 2 mission: A global geolocated photon product derived from the advanced topographic laser altimeter system. *Remote Sensing of Environment*, *233*, 111325. https://doi.org/10.1016/j.rse.2019.111325

Nick, F. M., Van Der Veen, C. J., Vieli, A., & Benn, D. I. (2010). A physically based calving model applied to marine outlet glaciers and implications for the glacier dynamics. *Journal of Glaciology*, *56*(199), 781–794. https://doi.org/10.3189/002214310794457344

Nowicki, S., Goelzer, H., Seroussi, H., Payne, A. J., Lipscomb, W. H., Abe-Ouchi, A., et al. (2020). Experimental protocol for sea level projections from ISMIP6 stand-alone ice sheet models. *The Cryosphere*, *14*(7), 2331–2368. https://doi.org/10.5194/tc-14-2331-2020

Nye, J. F. (1957). The distribution of stress and velocity in glaciers and ice-sheets. *Proceedings of the Royal Society of London. Series A*, *239*, 113–133.

Olinger, S. D., Lipovsky, B. P., & Denolle, M. A. (2024). Ocean coupling limits rupture velocity of fastest observed ice shelf rift propagation event. *AGU Advances*, *5*(1), e2023AV001023. https://doi.org/10.1029/2023AV001023

Paden, J., Li, J., Leuschen, C., Rodriguez-Morales, F., & Hale, R. (2010). IceBridge MCoRDS L2 ice thickness, version 1. *Distributed by NASA National Snow and Ice Data Center Distributed Active Archive Center*. https://doi.org/10.5067/GDQ0CUCVTE2Q

Paden, J., Li, J., Leuschen, C., Rodriguez-Morales, F., & Hale, R. (2014). IceBridge MCoRDS L1B geolocated radar echo strength profiles, version 2. *Distributed by NASA National Snow and Ice Data Center Distributed Active Archive Center*. https://doi.org/10.5067/90S1XZRBAX5N

Paolo, F. S., Padman, L., Fricker, H. A., Adusumilli, S., Howard, S., & Siegfried, M. R. (2018). Response of Pacific-sector Antarctic ice shelves to the El Niño/southern oscillation. *Nature Geoscience*, *11*(2), 121–126. https://doi.org/10.1038/s41561-017-0033-0

Parizek, B. R., Christianson, K., Anandakrishnan, S., Alley, R. B., Walker, R. T., Edwards, R. A., et al. (2013). Dynamic (in)stability of Thwaites Glacier, West Antarctica. *Journal of Geophysical Research: Earth Surface*, *118*(2), 638–655. https://doi.org/10.1002/jgrf.20044

Pollard, D., DeConto, R. M., & Alley, R. B. (2015). Potential Antarctic Ice Sheet retreat driven by hydrofracturing and ice cliff failure. *Earth and Planetary Science Letters*, *412*, 112–121. https://doi.org/10.1016/j.epsl.2014.12.035

Rabus, B. T., Lang, O., & Adolphs, U. (2003). Interannual velocity variations and recent calving of Thwaites Glacier Tongue, west Antarctica. *Annals of Glaciology*, *36*, 215–224. https://doi.org/10.3189/172756403781816176

Rankl, M., Fürst, J. J., Humbert, A., & Braun, M. H. (2017). Dynamic changes on the Wilkins Ice Shelf during the 2006–2009 retreat derived from satellite observations. *The Cryosphere*, *11*(3), 1199–1211. https://doi.org/10.5194/tc-11-1199-2017

Rignot, E., Mouginot, J., Morlighem, M., Seroussi, H., & Scheuchl, B. (2014). Widespread, rapid grounding line retreat of pine Island, thwaites, Smith, and Kohler Glaciers, West Antarctica, from 1992 to 2011. *Geophysical Research Letters*, *41*(10), 3502–3509. https://doi.org/10.1002/2014gl060140

Rignot, E., Mouginot, J., & Scheuchl, B. (2016). Measures Antarctic grounding line from differential satellite radar interferometry, version 2 [Dataset]. *NASA National Snow and Ice Data Center Distributed Active Archive Center*. https://doi.org/10.5067/IKBWW4RYHF1Q

Rignot, E., Mouginot, J., & Scheuchl, B. (2023). Measures grounding zone of the Antarctic ice sheet. (NSIDC-0778, version 1) [Dataset]. *NASA National Snow and Ice Data Center Distributed Active Archive Center*. https://doi.org/10.5067/HGLT8XB480E4

Ritz, C., Edwards, T. L., Durand, G., Payne, A. J., Peyaud, V., & Hindmarsh, R. C. A. (2015). Potential sea-level rise from Antarctic ice-sheet instability constrained by observations. *Nature*, *528*(7580), 115–118. https://doi.org/10.1038/nature16147

Robel, A. A., & Banwell, A. F. (2019). A speed limit on ice shelf collapse through hydrofracture. *Geophysical Research Letters*, *46*(21), 12092–12100. https://doi.org/10.1029/2019gl084397

Scambos, T. A., Bell, R. E., Alley, R. B., Anandakrishnan, S., Bromwich, D. H., Brunt, K., et al. (2017). How much, how fast?: A science review and outlook for research on the instability of Antarctica's Thwaites Glacier in the 21st century. *Global and Planetary Change*, *153*, 16–34. https://doi.org/10.1016/j.gloplacha.2017.04.008

Scambos, T. A., Bohlander, J. A., Shuman, C. A., & Skvarca, P. (2004). Glacier acceleration and thinning after ice shelf collapse in the Larsen B embayment, Antarctica. *Geophysical Research Letters*, *31*(18), L18402. https://doi.org/10.1029/2004gl020670

Scambos, T. A., Dutkiewicz, M. J., Wilson, J. C., & Bindschadler, R. A. (1992). Application of image cross-correlation to the measurement of glacier velocity using satellite image data. *Remote Sensing of Environment*, *42*(3), 177–186. https://doi.org/10.1016/0034-4257(92)90101-o

Schmidt, B. E., Washam, P., Davis, P. E. D., Nicholls, K. W., Holland, D. M., Lawrence, J. D., et al. (2023). Heterogeneous melting near the Thwaites Glacier grounding line. *Nature*, *614*(7948), 471–478. https://doi.org/10.1038/s41586-022-05691-0

Sergienko, O. (2025). Treatment of the ice-shelf backpressure and buttressing in two horizontal dimensions. *Journal of Glaciology*, *71*, e7. https://doi.org/10.1017/jog.2024.83

Seroussi, H., Nakayama, Y., Larour, E., Menemenlis, D., Morlighem, M., Rignot, E., & Khazendar, A. (2017). Continued retreat of Thwaites Glacier, West Antarctica, controlled by bed topography and ocean circulation. *Geophysical Research Letters*, *44*(12), 6191–6199. https://doi.org/10.1002/2017gl072910

Seroussi, H., Nowicki, S., Payne, A. J., Goelzer, H., Lipscomb, W. H., Abe-Ouchi, A., et al. (2020). ISMIP6 Antarctica: A multi-model ensemble of the Antarctic ice sheet evolution over the 21st century. *The Cryosphere*, *14*(9), 3033–3070. https://doi.org/10.5194/tc-14-3033-2020

Shean, D., Swinski, J. P., Smith, B., Sutterley, T., Henderson, S., Ugarte, C., et al. (2023). SlideRule: Enabling rapid, scalable, open science for the NASA ICESat-2 mission and beyond. *Journal of Open Source Software*, *8*(81), 4982. https://doi.org/10.21105/joss.04982

Smith, B., Adusumilli, S., Csathó, B. M., Felikson, D., Fricker, H. A., Gardner, A., et al., the ICESat-2 Science Team. (2021). ATLAS/ICESat-2 L3A land ice height, version 5 [Dataset]. *NASA National Snow and Ice Data Center Distributed Active Archive Center*. https://doi.org/10.5067/ATLAS/ATL06.005

Smith, B., Adusumilli, S., Csathó, B. M., Felikson, D., Fricker, H. A., Gardner, A. S., et al., the ICESat-2 Science Team (2023). ATLAS/ICESat-2 L3A land ice height. (ATL06, version 6) [Dataset]. *NASA National Snow and Ice Data Center Distributed Active Archive Center*. https://doi.org/10.5067/ATLAS/ATL06.006

Smith, B., Fricker, H. A., Gardner, A. S., Medley, B., Nilsson, J., Paolo, F. S., et al. (2020). Pervasive ice sheet mass loss reflects competing ocean and atmosphere processes. *Science*, *368*(6496), 1239–1242. https://doi.org/10.1126/science.aaz5845

Smith, B., Fricker, H. A., Holschuh, N., Gardner, A. S., Adusumilli, S., Brunt, K. M., et al. (2019). Land ice height-retrieval algorithm for NASA's ICESat-2 photon-counting laser altimeter. *Remote Sensing of Environment*, *233*, 111352. https://doi.org/10.1016/j.rse.2019.111352

Soci, C., Hersbach, H., Simmons, A., Poli, P., Bell, B., Berrisford, P., et al. (2024). The ERA5 global reanalysis from 1940 to 2022. *Quarterly Journal of the Royal Meteorological Society*, *150*(764), 4014–4048. https://doi.org/10.1002/qj.4803

Sun, S., Cornford, S. L., Moore, J. C., Gladstone, R., & Zhao, L. (2017). Ice shelf fracture parameterization in an ice sheet model. *The Cryosphere*, *11*(6), 2543–2554. https://doi.org/10.5194/tc-11-2543-2017

Surawy-Stepney, T., Hogg, A. E., Cornford, S. L., & Davison, B. J. (2023). Episodic dynamic change linked to damage on the Thwaites Glacier Ice Tongue. *Nature Geoscience*, *16*(1), 37–43. https://doi.org/10.1038/s41561-022-01097-9

Thoma, M., Jenkins, A., Holland, D., & Jacobs, S. (2008). Modelling circumpolar deep water intrusions on the Amundsen Sea continental shelf, Antarctica. *Geophysical Research Letters*, *35*(18), L18602. https://doi.org/10.1029/2008GL034939

Torres, R., Navas-Traver, I., Bibby, D., Lokas, S., Snoeij, P., Rommen, B., et al. (2017). Sentinel-1 SAR system and mission. In *2017 IEEE radar conference (RadarConf)*. IEEE. https://doi.org/10.1109/radar.2017.7944460

van der Veen, C. J. (1998). Fracture mechanics approach to penetration of surface crevasses on glaciers. *Cold Regions Science and Technology*, *27*(1), 31–47. https://doi.org/10.1016/s0165-232x(97)00022-0

Veci, L., Prats-Iraola, P., Scheiber, R., Collard, F., Fomferra, N., & Engdahl, M. (2014). The sentinel-1 toolbox. In *Proceedings of the IEEE international geoscience and remote sensing symposium (IGARSS)* (pp. 1–3). IEEE.

Wåhlin, A. K., Graham, A. G. C., Hogan, K. A., Queste, B. Y., Boehme, L., Larter, R. D., et al. (2021). Pathways and modification of warm water flowing beneath Thwaites ice shelf, West Antarctica. *Science Advances*, *7*(15). https://doi.org/10.1126/sciadv.abd7254

Walker, C. C., Becker, M. K., & Fricker, H. A. (2021). A high resolution, three-dimensional view of the D-28 calving event from Amery ice shelf with ICESat-2 and satellite imagery. *Geophysical Research Letters*, *48*(3). https://doi.org/10.1029/2020gl091200

Walker, C. C., & Gardner, A. S. (2019). Evolution of ice shelf rifts: Implications for formation mechanics and morphological controls. *Earth and Planetary Science Letters*, *526*, 115764. https://doi.org/10.1016/j.epsl.2019.115764

Walker, D. P., Brandon, M. A., Jenkins, A., Allen, J. T., Dowdeswell, J. A., & Evans, J. (2007). Oceanic heat transport onto the Amundsen Sea shelf through a submarine glacial trough. *Geophysical Research Letters*, *34*(2), L02602. https://doi.org/10.1029/2006GL028154

Wang, S., Alexander, P., Alley, R. B., Huang, Z., Parizek, B. R., Willet, A., et al. (2024). Thwaites Ice Shelf fracture depth-to-freeboard ratios, flow velocities, strain rates (2018-2024) [Dataset]. *figshare*. https://doi.org/10.6084/m9.figshare.27129105.v2

Wang, S., Alexander, P., Wu, Q., Tedesco, M., & Shu, S. (2021). Characterization of ice shelf fracture features using ICESat-2 – a case study over the Amery Ice Shelf. *Remote Sensing of Environment*, *255*, 112266. https://doi.org/10.1016/j.rse.2020.112266

Wang, S., Liu, H., Alley, R. B., Jezek, K., Alexander, P., Alley, K. E., et al. (2023). Multidecadal pre- and post-collapse dynamics of the Northern Larsen Ice Shelf. *Earth and Planetary Science Letters*, *609*, 118077. https://doi.org/10.1016/j.epsl.2023.118077

Wang, S., Liu, H., Jezek, K., Alley, R. B., Wang, L., Alexander, P., & Huang, Y. (2022). Controls on Larsen C ice shelf retreat from a 60-year satellite data record. *Journal of Geophysical Research: Earth Surface*, *127*(3). https://doi.org/10.1029/2021jf006346

Wang, S., Liu, H., Yu, B., Zhou, G., & Cheng, X. (2016). Revealing the early ice flow patterns with historical declassified intelligence satellite photographs back to 1960s. *Geophysical Research Letters*, *43*(11), 5758–5767. https://doi.org/10.1002/2016gl068990

Wang, S., Wu, Q., & Ward, D. (2017). Automated delineation and characterization of drumlins using a localized contour tree approach. *International Journal of Applied Earth Observation and Geoinformation*, *62*, 144–156. https://doi.org/10.1016/j.jag.2017.06.006

Watkins, R. H., Bassis, J. N., & Thouless, M. D. (2021). Roughness of ice shelves is correlated with basal melt rates. *Geophysical Research Letters*, *48*(21), e2021GL094743. https://doi.org/10.1029/2021gl094743

Watkins, R. H., Bassis, J. N., Thouless, M. D., & Luckman, A. (2024). High basal melt rates and high strain rates lead to more fractured ice. *Journal of Geophysical Research: Earth Surface*, *129*(4), e2023JF007366. https://doi.org/10.1029/2023jf007366

Weertman, J. (1973). Can a water-filled crevasse reach the bottom surface of a glacier. *IASH Publ*, *95*, 139–145.

Wild, C. T., Alley, K. E., Muto, A., Truffer, M., Scambos, T. A., & Pettit, E. C. (2022). Weakening of the pinning point buttressing Thwaites Glacier, West Antarctica. *The Cryosphere*, *16*(2), 397–417. https://doi.org/10.5194/tc-16-397-2022

Wild, C. T., Kachuck, S. B., Luckman, A., Alley, K. E., Sharp, M. A., Smith, H., et al. (2024). Rift propagation signals the last act of the Thwaites Eastern Ice Shelf despite low basal melt rates. *Journal of Glaciology*, *70*, 1–18. https://doi.org/10.1017/jog.2024.64

Wu, Q., Liu, H., Wang, S., Yu, B., Beck, R., & Hinkel, K. (2015). A localized contour tree method for deriving geometric and topological properties of complex surface depressions based on high-resolution topographical data. *International Journal of Geographical Information Science: IJGIS*, *29*(12), 2041–2060. https://doi.org/10.1080/13658816.2015.1038719

Zuo, H., Balmaseda, M. A., Tietsche, S., Mogensen, K., & Mayer, M. (2019). The ECMWF operational ensemble reanalysis–analysis system for ocean and sea ice: A description of the system and assessment. *Ocean Science*, *15*(3), 779–808. https://doi.org/10.5194/os-15-779-2019

References From the Supporting Information

Cuffey, K. M., & Paterson, W. S. B. (2010). *The physics of glaciers*. Academic Press.

Morlighem, M. (2022). Measures Bed Machine Antarctica, version 3 [Dataset]. *NASA National Snow and Ice Data Center Distributed Active Archive Center*. https://doi.org/10.5067/FPSU0V1MWUB6